Dual-slope method for enhanced depth sensitivity in diffuse optical spectroscopy

Angelo Sassaroli[*], **Giles Blaney**, **Sergio Fantini**

Department of Biomedical Engineering, Tufts University, 4 Colby Street, Medford, Massachusetts 02155, USA

Abstract

Using diffusion theory, we show that a dual-slope method is more effective than single-slope methods or single-distance methods at enhancing sensitivity to deeper tissue. The dual-slope method requires a minimum of two sources and two detectors arranged in specially configured arrays. In particular, we present diffusion theory results for a symmetrical linear array of two sources (separated by 55 mm) that sandwich two detectors (separated by 15 mm), for which dual slopes achieve maximal sensitivity at a depth of about 5 mm for direct current (DC) intensity (as measured in continuous-wave spectroscopy) and 11 mm for phase (as measured in frequency-domain spectroscopy) under typical values of the tissue optical properties (absorption coefficient: ~0.01 mm^{-1}, reduced scattering coefficient: ~1 mm^{-1}). This result is a major advance over single-distance or single-slope data, which feature maximal sensitivity to shallow tissue (<2 mm for the intensity, <5 mm for the phase).

1. INTRODUCTION

Near-infrared spectroscopy (NIRS) in the wavelength range 700–1000 nm finds applications in the noninvasive study of biological tissue over macroscopic spatial scales of millimeters to centimeters. Applications include functional brain imaging [1]; cerebral oximetry [2,3]; stroke [4]; neonatal cerebral, liver, gastro-intestinal, and peripheral oximetry [5]; skeletal muscle flow and oxygen consumption [6]; and optical mammography [7]. An important question for these noninvasive, diffuse optical measurements is the spatial extent of the probed tissue volume. In other words, what is the interrogated tissue volume, and how is the sensitivity of the measured signal distributed within this volume? These questions become especially important in the investigation of deeper tissue, say the brain or skeletal muscle, where superficial tissue (scalp, skull, skin, adipose layer, etc.) may provide confounding contributions to the measured optical signal. This paper studies this question for a variety of single-distance and multi-distance source-detector configurations, as well as for optical measurements in continuous-wave spectroscopy (DC, or direct current intensity) or in the frequency domain (AC, or alternating current amplitude, and phase).

As an alternative to sophisticated forward models of photon migration and even more computationally demanding inversion procedures in diffuse optical spectroscopy (e.g.,

---

[*]Corresponding author: angelo.sassaroli@tufts.edu.

diffuse optical tomography) [8], we investigate the possibility of using simple functions of optical data types collected with special source-detector arrangements to enhance the sensitivity to deeper tissue regions and to spatially confine the region of sensitivity. Homogeneous models of photon migration are used for the data inversion by using the concept of equivalent absorption change. We show how in general it is possible to retrieve changes in the absorption coefficient by using different data types (and derived single or dual slopes) independently. This method has the advantage of not mixing data types with different features of spatial sensitivity. While this approach does not aim at solving the full inverse imaging problem, it can result in a robust approach to diffuse optical imaging of deep tissue. We focus on the slopes (or gradients versus source-detector separation) of three fundamental data types in frequency-domain NIRS (DC, AC, and phase), and we show how they can offer a better sensitivity to deeper tissue regions than data collected at a single source-detector separation. NIRS data slopes versus source-detector separation have been proposed for absolute measurements of tissue optical properties [9–11], for measurements of a tissue oxygenation index [12,13], and for reduced sensitivity to superficial layers [14]. Here we exploit the reduced sensitivity of multi-distance data to superficial layers, and we also take into consideration the different spatial distribution of the intensity and phase regions of sensitivities.

To avoid a number of drawbacks associated with the slopes obtained from single-source or single-detector configurations (which we identify as "single slopes" here), we propose the use of special source-detector arrays to measure two slopes and average them (we identify this approach as a "dual-slope" method). This dual-slope method features: (1) insensitivity to instrumental effects related to temporal variations in source emission and detector sensitivity properties; (2) insensitivity to changes in optical coupling between optical probe and tissue; (3) reduced sensitivity to localized as well as uniform superficial tissue inhomogeneities, resulting in a greater relative sensitivity to deeper tissue; and (4) localized sensitivity to a deep tissue volume, which does not feature the typical banana shape of NIRS regions of sensitivity. Similar symmetrical source-detector arrays were previously proposed for self-calibrating measurements of the absolute optical properties of homogenous media, demonstrating their effectiveness in achieving points (1) and (2) [15]. Also, DC measurements based on the self-calibrating approach (with the assumption of a wavelength-independent reduced scattering coefficient) were translated into oxygen saturation measurements either on phantoms or *in vivo* human studies [16–20]. Self-calibrating DC measurements (with assumed values of the reduced scattering coefficient) have also been used for measuring changes in oxy- and deoxyhemoglobin concentrations in human or animal studies [18,21–23]. Finally, self-calibrating methods with DC measurements have been used to show their effectiveness in removing motion artifacts [24,25]. Some of the above studies mention the insensitivity of the self-calibrating approach to skin marks or other superficial inhomogeneities [16,19] and also to superficial tissue such as scalp and skull [17,18], but no quantitative descriptions have been previously provided, nor were AC and phase data considered.

In this work, we carry out a detailed theoretical study of the sensitivity of single-distance versus single-slope and dual-slope methods (based on DC, AC, and phase data types) to focal absorption perturbations, which proves points (3) and (4) above. The results show how

the dual-slope method is an effective approach to sense deeper tissue (for example, brain cortex) with minimal sensitivity to superficial tissue (for example, scalp) and instrumental artifacts. In particular, we show how phase dual slopes feature a more specific sensitivity to deeper tissue than intensity dual slopes. However, a drawback of phase measurements is their lower signal-to-noise ratio compared to intensity measurements. For cases of lower optical contrast, or for instruments that do not collect frequency-domain data, dual DC intensity slopes may be used, as they are still preferable over single slopes, but they would feature maximal sensitivity to shallower tissue than dual-phase slopes. Other theoretical computations were run to establish if the dual-slope method can correctly retrieve relative changes of oxy- and deoxyhemoglobin concentrations occurring in the brain in typical brain studies. We chose two scenarios: (a) a typical protocol of coherent hemodynamic spectroscopy [26] and (b) a typical brain activation case [27]. In the first case, systemic oscillatory hemodynamic changes are induced both in the extracerebral layer and in the brain rather uniformly, so in the simulations we have assumed layered changes in the absorption coefficients. In the second case, we have assumed more localized absorption changes deeper in the tissue and some absorption changes in the outer layer. The results show how the dual-slope method (in particular with phase data) can effectively retrieve the relative changes of oxy- and deoxyhemoglobin in deeper tissues.

2. THEORY

We start with fundamental formulas for the sensitivity of DC (direct current intensity), AC (alternating current amplitude) and phase (φ), measured at a single source-detector separation, to focal absorption changes within an arbitrary diffusing and absorbing medium (Section 2.A). We then proceed by deriving the sensitivity of the single slopes of these data types (where the independent variable is the source-detector separation) to focal absorption changes (Section 2.B). The derived formulas are general regardless of the geometry and optical heterogeneity of the medium. In a geometry of semi-infinite homogeneous diffusive medium it was demonstrated that $\ln(r^2\mathrm{DC}(r))$, $\ln(r^2\mathrm{AC}(r))$, and $\varphi(r)$, where r is the source-detector separation, are well approximated by straight lines [28]. In this work, we make the (reasonable) hypothesis that these properties are valid also for many types of real tissues if the measurements are carried out in a reflectance geometry, which is assumed in this work. Of course, in general the slope of a straight line and the way it changes in dynamic and heterogeneous conditions will not depend only on the source-detector separations but also on the source-detector arrangement on the tissue surface. In the following section, we address the sensitivity of a data type measured at a single distance or its slope to focal hemoglobin changes (Section 2.C). Then we introduce the method of the dual slope with two different types of source-detector arrangements (Section 2.D), and we provide the equations used for the numerical results of this work (Section 2.E). Finally, in Section 2.F we discuss the topic of noise-to-signal ratio (NSR) for the different methods. In the following sections, as a mathematical convention, a variable in bold means that the variable represents a position vector in the space, while an arrow on top of a variable indicates that the variable is not a vector in space, but an array of a specified dimension.

A.   Spatial Sensitivity of Raw Data Types (DC, AC, and Phase) at a Single Source-Detector Separation

Within first-order perturbation theory of the diffusion equation (DE) [29], one can write

$$\frac{1}{\text{DC}(\mathbf{r}_s, \mathbf{r}_d)} \frac{\partial \text{DC}(\mathbf{r}_s, \mathbf{r}_d)}{\partial \mu_{ak}} = -\langle l \rangle (\mathbf{r}_s, \mathbf{r}_k, \mathbf{r}_d) = -\langle l_{\text{DC}} \rangle (\mathbf{r}_s, \mathbf{r}_k, \mathbf{r}_d),$$ (1)

where $\mathbf{r}_s$ is the position vector of a point source; $\text{DC}(\mathbf{r}_s, \mathbf{r}_d)$ is the detected direct current intensity at the detector position $\mathbf{r}_d$; μ_{ak} is the absorption coefficient of a region (labeled k) within the diffusive medium, which is identified by the position vector $\mathbf{r}_k$; and $\langle l \rangle (\mathbf{r}_s, \mathbf{r}_k, \mathbf{r}_d)$ is the average partial path length traveled inside region k by photons emitted at $\mathbf{r}_s$ detected at $\mathbf{r}_d$. In two previous works, we have reframed the perturbation theory of DE by using the path length moments in the three domains [continuous wave (CW), frequency domain (FD), and time domain (TD)] of near-infrared spectroscopy (NIRS), and we showed that the following formula similar to Eq. (1) is valid also for the FD reflectance [30]:

$$\frac{1}{\widetilde{R}(\mathbf{r}_s, \mathbf{r}_d, \omega)} \frac{\partial \widetilde{R}(\mathbf{r}_s, \mathbf{r}_d, \omega)}{\partial \mu_{ak}} = -\langle \tilde{l} \rangle (\mathbf{r}_s, \mathbf{r}_k, \mathbf{r}_d, \omega),$$ (2)

where $\widetilde{R}(\mathbf{r}_s, \mathbf{r}_d, \omega) = \text{AC}(\mathbf{r}_s, \mathbf{r}_d, \omega) \exp(i\varphi(\mathbf{r}_s, \mathbf{r}_d, \omega))$ is the complex notation for the reflectance measured at $\mathbf{r}_d$, and $\langle \tilde{l} \rangle$ is the associated complex path length, which reduces to the usual path length of Eq. (1) when the angular modulation frequency (ω) is zero. In fact, Eq. (2) reduces to Eq. (1) for $\omega = 0$. One can easily verify that Eq. (2) implies two separate equations for AC and φ as follows:

$$\frac{1}{\text{AC}(\mathbf{r}_s, \mathbf{r}_d, \omega)} \frac{\partial \text{AC}(\mathbf{r}_s, \mathbf{r}_d, \omega)}{\partial \mu_{ak}} = -\text{Re}\left[\langle \tilde{l} \rangle (\mathbf{r}_s, \mathbf{r}_k, \mathbf{r}_d, \omega)\right] = -\langle l_{\text{AC}} \rangle (\mathbf{r}_s, \mathbf{r}_k, \mathbf{r}_d, \omega),$$ (3)

$$\frac{\partial \varphi(\mathbf{r}_s, \mathbf{r}_d, \omega)}{\partial \mu_{ak}} = -\text{Im}\left[\langle \tilde{l} \rangle (\mathbf{r}_s, \mathbf{r}_k, \mathbf{r}_d, \omega)\right] = -\langle l_\varphi \rangle (\mathbf{r}_s, \mathbf{r}_k, \mathbf{r}_d, \omega),$$ (4)

where "Re" and "Im" are the real and imaginary part of a complex number, respectively. An approximate formula for $\langle \tilde{l} \rangle (\mathbf{r}_s, \mathbf{r}_k, \mathbf{r}_d, \omega)$ is given by [30]

$$\langle \tilde{l} \rangle (\mathbf{r}_s, \mathbf{r}_k, \mathbf{r}_d, \omega), \cong \frac{\widetilde{\Phi}(\mathbf{r}_s, \mathbf{r}_k, \omega) \widetilde{R}(\mathbf{r}_s, \mathbf{r}_d, \omega)}{\widetilde{R}(\mathbf{r}_s, \mathbf{r}_d, \omega)} V_k,$$ (5)

where $\widetilde{\Phi}(\mathbf{r}_s, \mathbf{r}_k, \omega)$, $\widetilde{R}(\mathbf{r}_k, \mathbf{r}_d, \omega)$, and $\widetilde{R}(\mathbf{r}_s, \mathbf{r}_d, \omega)$ are the FD Green's function of fluence calculated at $\mathbf{r}_k$ when photons are emitted from $\mathbf{r}_s$, the FD reflectance (output intensity) measured at the detector's point $\mathbf{r}_d$ when photons are emitted from $\mathbf{r}_k$, and the FD reflectance measured at the detector's point $\mathbf{r}_d$ when photons are emitted from $\mathbf{r}_s$, respectively. V_k is the volume of the k region ("centered" at $\mathbf{r}_k$) where a change in absorption occurs. Note that Eq. (5) is valid if the maximum linear size of the region (labeled k) is much smaller than $|\mathbf{r}_s - \mathbf{r}_k|$ and $|\mathbf{r}_d - \mathbf{r}_k|$. If this approximation is not valid, the correct calculation of the partial path length requires a volume integration [30].

The complex partial path length can be qualitatively interpreted as the fraction of the photon density wave detected at $\mathbf{r}_d$ that reaches the region at $\mathbf{r}_k$. Because photon density waves are exponentially damped as a function of the modulation frequency, as we increase ω a smaller wave fraction will reach the k region before being detected. On the contrary, for the limiting case $\omega = 0$ (DC case) the partial pathlength depends only on geometrical conditions and optical properties. We want to rewrite Eqs. (1), (3), and (4) in a concise way with a single formula (where the dependence on ω is implicit) as follows:

$$\frac{\overline{\partial Y}(\mathbf{r}_s, \mathbf{r}_d)}{\partial \mu_{ak}} = -\langle l_Y \rangle (\mathbf{r}_s, \mathbf{r}_k, \mathbf{r}_d), \tag{6}$$

where "Y" is a data type (DC, AC, or φ); the bar on the top of the derivative means that the derivative is normalized, in the DC and AC cases, by dividing by DC or AC, respectively [as in Eqs. (1) and (3)]; and $\langle l_Y \rangle (\mathbf{r}_s, \mathbf{r}_k, \mathbf{r}_d)$ is the pathlength corresponding to the Y data type [as in Eqs. (1), (3), and (4)] when the focal change occurs at $\mathbf{r}_k$, the photons are emitted at $\mathbf{r}_s$, and they are detected at $\mathbf{r}_d$.

If we have M distinct focal changes in the absorption coefficient, within first-order perturbation theory (which assumes independent, i.e., non-interacting focal absorption changes) we can express the total change of the normalized data type as the sum of contributions due to each focal change as

$$\overline{\Delta Y}(\mathbf{r}_s, \mathbf{r}_d) = -\sum_{k=1}^{M} \langle l_Y \rangle (\mathbf{r}_s, \mathbf{r}_k, \mathbf{r}_d) \Delta \mu_{ak}. \tag{7}$$

Many sophisticated algorithms [8] target the reconstruction of the true focal absorption changes $\Delta \mu_{ak}$ by measuring $\overline{\Delta Y}(\mathbf{r}_s, \mathbf{r}_d)$ for multiple source-detector pairs on the medium boundary and using computationally complex inversion procedures. In this work, we study the "equivalent" homogeneous absorption change that yields the same $\overline{\Delta Y}(\mathbf{r}_s, \mathbf{r}_d)$ that is associated with a collection of M localized absorbers. In fact, based on Eq. (6), if we assume that $\overline{\Delta Y}(\mathbf{r}_s, \mathbf{r}_d)$ arises from a homogeneous absorption change in the medium, we have

$$\overline{\Delta Y}(\mathbf{r}_s, \mathbf{r}_d) = -\langle L_Y \rangle (\mathbf{r}_s, \mathbf{r}_d) \Delta \mu_{aY}(\mathbf{r}_s, \mathbf{r}_d), \tag{8}$$

where $\langle L_Y \rangle (\mathbf{r}_s, \mathbf{r}_d)$ is the average total path length traveled (in the whole medium) by photons emitted at $\mathbf{r}_s$ and detected at $\mathbf{r}_d$ for data type Y, and $\Delta \mu_{aY}(\mathbf{r}_s, \mathbf{r}_d)$ is the equivalent homogeneous absorption change estimated by data type Y {we note that when $Y = $ DC, Eq. (8) is the modified Beer–Lambert law [31,32]}. The equivalent homogeneous absorption change is related to the set of M true absorption changes by the relationship

$$\Delta \mu_{aY}(\mathbf{r}_s, \mathbf{r}_d) = \sum_{k=1}^{M} \frac{\langle l_Y \rangle (\mathbf{r}_s, \mathbf{r}_k, \mathbf{r}_d)}{\langle L_Y \rangle (\mathbf{r}_s, \mathbf{r}_d)} \Delta \mu_{ak}. \tag{9}$$

For a single focal change in absorption at $\mathbf{r}_k$, we define the sensitivity (S) of data type Y detected at $\mathbf{r}_d$ as follows:

$$S_Y(\mathbf{r}_s, \mathbf{r}_k, \mathbf{r}_d) = \frac{\langle l_Y \rangle (\mathbf{r}_s, \mathbf{r}_k, \mathbf{r}_d)}{\langle L_Y \rangle (\mathbf{r}_s, \mathbf{r}_d)} = \frac{\Delta \mu_{aY}(\mathbf{r}_s, \mathbf{r}_d)}{\Delta \mu_{ak}}. \tag{10}$$

We note that $S_Y(\mathbf{r}_s, \mathbf{r}_d)$ is always positive for DC data because $\langle l_{DC} \rangle (\mathbf{r}_s, \mathbf{r}_k, \mathbf{r}_d)$ and $\langle L_{DC} \rangle (\mathbf{r}_s, \mathbf{r}_d)$ represent the actual physical mean partial and total path lengths, respectively. This is true also for AC data, at least for typical values of ω used in NIRS [even though $\langle l_{AC} \rangle (\mathbf{r}_s, \mathbf{r}_k, \mathbf{r}_d)$ and $\langle L_{AC} \rangle (\mathbf{r}_s, \mathbf{r}_d)$ do not represent mean physical path lengths], but this is not generally true for phase data. Therefore, given a single focal change ($\Delta \mu_{ak}$), the equivalent homogeneous absorption change estimated with DC and AC data ($\Delta \mu_{aDC}$, $\Delta \mu_{aAC}$) will always have the same sign of the true change, while this is not always the case for phase data. The behavior of phase data with respect to a focal absorption change can be understood if we consider that, for typical modulation frequencies used in NIRS such that $\omega \ll v \mu_a$ (where v is the speed of light in the medium), $\varphi(\mathbf{r}_s, \mathbf{r}_d) \cong (\omega/v) \langle L_{DC} \rangle (\mathbf{r}_s, \mathbf{r}_d)$. If we consider a focal absorption increase occurring deeper in tissue, photons travelling along longer paths will have a higher chance to be absorbed, and the overall effect will be a shortening of $\langle L_{DC} \rangle (\mathbf{r}_s, \mathbf{r}_d)$ and therefore a decrease of phase. If an absorption increase occurs closer to the medium boundary, the effect on phase is more complex, and it is possible that photons with shorter path lengths be preferentially absorbed, resulting in an increase in $\langle L_{DC} \rangle (\mathbf{r}_s, \mathbf{r}_d)$ and therefore an increase of phase. A more rigorous reasoning is based on the observation that the change in phase due to a focal change in absorption depends on both the variance of the path lengths inside the focal region and the covariance of the path lengths travelled inside and outside the region. While the variance is always positive, the covariance can be either positive or negative [33] and may prevail on the other term. However, we observe that a homogenous increase in absorption will always cause a decrease in phase. These properties can be summarized by saying that, in the case of an absorption increase: $\langle l_\varphi \rangle (\mathbf{r}_s, \mathbf{r}_k, \mathbf{r}_d)$ maybe >0, <0, or = 0, whereas $\langle L_\varphi \rangle (\mathbf{r}_s, \mathbf{r}_d)$ is always >0. The fact that $\langle L_\varphi \rangle$ is always >0 is linked to the definition of $\langle L_{DC} \rangle$, where the pathlength of each detected photon (L) is weighted by the factor $e^{-\mu_a L}$, which penalizes photons traveling longer paths with respect to photons traveling shorter paths. Therefore, as we uniformly increase the absorption coefficient of the whole medium, $\langle L_{DC} \rangle$ decreases, and so does the phase (this statement can be proven mathematically by using the properties of the radiative transfer equation). We stress that all the equations written in this section are general, regardless of the geometry of the medium (except media with concave boundaries) and heterogeneity of the optical properties. The only assumption is the validity of the first-order perturbation theory of the DE. In a practical situation, the equivalent absorption change is found by inverting Eq. (8), which requires the knowledge of the total path lengths. For particular geometries, like the semi-infinite homogeneous medium geometry, the total path lengths are easily calculated once one knows the absolute optical properties of the medium (see Section 2.E).

B. Spatial Sensitivity of Single Slopes of DC, AC, and Phase

In this section, we simplify the notation by using scalar source-detector distances (r_i) instead of position vectors for one source ($\mathbf{r}_s$) and multiple detectors ($\mathbf{r}_{di}$ where $i = 1, ..., N$), which are on the tissue surface. In other words, $r_i = |\mathbf{r}_s - \mathbf{r}_{di}|$ will be used instead of the whole set of position vectors for the source and the detectors. However, we note that in a heterogeneous

medium (like we are assuming) the partial and total path lengths when photons are collected at $\mathbf{r}_{di}$ depends on both $\mathbf{r}_s$ and $\mathbf{r}_{di}$ (and on $\mathbf{r}_k$ for the partial path lengths) and not only on the distance r_i. We will only retain the three-dimentional (3D) position vectors that identify the focal regions where absorption changes occur. We want to provide formulas for the sensitivity of the slopes of $\ln(r^2 DC(r))$, $\ln(r^2 AC(r))$, and $\varphi(r)$ to focal absorption changes. The general solution for the best straight line (in a least-squares sense) through N points having coordinates (x_i, y_i) where $i = 1, \ldots, N$ yields a slope equal to $\text{cov}(\overrightarrow{x}, \overrightarrow{y})/\text{var}(\overrightarrow{x})$, where "cov" and "var" are the covariance and variance, respectively. In our case, $x_i = r_i$ is a set of N source-detector separations (with respect to a single source) and $y_i = y(r_i)$ is $\ln\left[r_i^2 DC(r_i)\right]$, $\ln\left[r_i^2 AC(r_i)\right]$, or $\varphi(r_i)$, which can be considered new data types ("y") derived from the "Y" data types. More specifically, in this section we consider slopes that are obtained using a single source and multiple detectors (or, equivalently, a single detector and multiple sources), and we refer to these slopes as "single slopes." Therefore, by indicating the single slope of data type "y" as "SSl_Y," one can write

$$SSl_Y = \frac{\text{cov}(\overrightarrow{r}, \overrightarrow{y})}{\text{var}(\overrightarrow{r})}. \tag{11}$$

If we now calculate the derivative of Eq. (11) with respect to a focal change in absorption at $(\mathbf{r}_k)$, after some algebra we find

$$\frac{\partial SSl_Y(\mathbf{r}_k, \overrightarrow{r})}{\partial \mu_{ak}} = -\frac{(\overrightarrow{r} - \overrightarrow{\langle r \rangle})\overrightarrow{\langle l_Y \rangle}(\mathbf{r}_k, \overrightarrow{r})}{N\text{var}(\overrightarrow{r})}, \tag{12}$$

where $\langle \overrightarrow{r} \rangle$ is the average source-detector separation $(\langle \overrightarrow{r} \rangle = \sum_{i=1}^{N} r_i / N)$, $(\overrightarrow{r} - \overrightarrow{\langle r \rangle})$ is a $1 \times N$ array with elements $r_i - \langle \overrightarrow{r} \rangle$, $\overrightarrow{\langle l_Y \rangle}(\mathbf{r}_k, \overrightarrow{r})$ is an $N \times 1$ array with elements $\langle l_Y \rangle(\mathbf{r}_k, r_i)$, and $\text{var}(\overrightarrow{r}) = \langle | \overrightarrow{r} - \overrightarrow{\langle r \rangle} |^2 \rangle$. We observe again that $\langle l_Y \rangle(\mathbf{r}_k, r_i)$ is a simplified notation for $\langle l_Y \rangle$ $(\mathbf{r}_s, \mathbf{r}_k, \mathbf{r}_{di})$, where $i = 1, \ldots, N$. In the derivation of Eq. (12), we have used Eqs. (2)–(4) and the property that $\frac{\partial y_i}{\partial \mu_{ak}} = \left(\frac{\overline{\partial Y(r_i)}}{\partial \mu_{ak}}\right) = -\langle l_Y \rangle(\mathbf{r}_k, r_i)$. Within first-order perturbation theory, we can easily derive the change in the slope of a data type due to M focal absorbers at r_k, where $k = 1, \ldots, M$, as follows:

$$\Delta SSl_Y(\overrightarrow{r}) = \frac{(\overrightarrow{r} - \overrightarrow{\langle r \rangle})\widehat{\langle l_Y \rangle}\overrightarrow{\Delta \mu_a}}{N\text{var}(\overrightarrow{r})}, \tag{13}$$

where $\widehat{\langle l_Y \rangle}$ is an $N \times M$ matrix [with elements $\langle l_Y \rangle(\mathbf{r}_k, r_i)$], and $\overrightarrow{\Delta \mu_a}$ is an $M \times 1$ absorption change array (with elements $\Delta \mu_{ak}$). We note that $\overrightarrow{\langle l_Y \rangle}(\mathbf{r}_k, \overrightarrow{r})$ of Eq. (12) is the k th column of $\widehat{\langle l_Y \rangle}$. Similarly to Eq. (7) for the raw data types, Eq. (13) shows how the changes in the slope of a data type are related to the true localized changes in the absorption coefficients in the medium. Also, for the slopes, we can estimate an equivalent homogeneous absorption change ($\Delta \mu_{aY}$) associated with ΔSSl_Y that satisfies the equation

$$\Delta SSl_Y(\mathbf{r}_s, \overrightarrow{r}) = -\frac{(\overrightarrow{r} - \overrightarrow{\langle r \rangle})\overrightarrow{\langle L_Y \rangle}(\overrightarrow{r})\Delta\mu_{aY}(\overrightarrow{r})}{N\mathrm{var}(\overrightarrow{r})},$$ (14)

where $\overrightarrow{\langle L_Y \rangle}(\overrightarrow{r})$ is an $N \times 1$ array with elements $\langle L_Y \rangle(r_i)$, where $i = 1, \ldots, N$. In this case, we note that the homogeneous equivalent absorption change $\Delta\mu_{aY}(\overrightarrow{r})$ depends not only on the data type (Y) but also on the set of source-detector distances $(\overrightarrow{r})$. The relationship between the true focal absorption changes and $\Delta\mu_{aY}$ is easily derived as

$$\Delta\mu_{aY}(\overrightarrow{r}) = \frac{(\overrightarrow{r} - \overrightarrow{\langle r \rangle})\overrightarrow{\langle \widehat{l_Y} \rangle}\overrightarrow{\Delta\mu_a}}{(\overrightarrow{r} - \overrightarrow{\langle r \rangle})\overrightarrow{\langle L_Y \rangle}(\overrightarrow{r})}.$$ (15)

Based on Eq. (15), one can define the sensitivity of the single slope of a data type (where the set of source-detector distances $\overrightarrow{r}$ is used) with respect to a focal absorption change at $\mathbf{r}_k$ as

$$S_{SSl_Y}(\mathbf{r}_k, \overrightarrow{r}) = -\frac{(\overrightarrow{r} - \overrightarrow{\langle r \rangle})\overrightarrow{\langle l_Y \rangle}(\mathbf{r}_k, \overrightarrow{r})}{(\overrightarrow{r} - \overrightarrow{\langle r \rangle})\overrightarrow{\langle L_Y \rangle}(\overrightarrow{r})} = \frac{\Delta\mu_{aY}(\overrightarrow{r})}{\Delta\mu_{ak}}.$$ (16)

We note that similarly to the sensitivity of the phase data type, the sensitivity of the slopes of the three data types can also be either positive or negative. This can be easily seen for the simple case of two source-detector separations r_1 and r_2 (with $r_2 > r_1$) and one focal change at $\mathbf{r}_k$. In this case, Eq. (16) becomes

$$S_{SSl_Y}(\mathbf{r}_k, \overrightarrow{r}) = \frac{\langle l_Y \rangle(\mathbf{r}_k, r_2) - \langle l_Y \rangle(\mathbf{r}_k, r_1)}{\langle L_Y \rangle(r_2) - \langle L_Y \rangle(r_1)}.$$ (17)

The interpretation of Eq. (17) is easier for the DC or AC data type. In this case, for focal changes of the absorption coefficient, the denominator is always positive, while the numerator can be either positive or negative. For example, if a focal change occurs in proximity of the detector at r_1 [where $\langle l_Y \rangle(\mathbf{r}_k, r_1) > \langle l_Y \rangle(\mathbf{r}_k, r_2)$], the sensitivity becomes negative. If a focal change occurs in proximity of r_2 or deeper in the tissue, the sensitivity is positive. Also, there are deep regions of the medium where the slope method has a higher sensitivity to focal absorption changes than that of the corresponding data type [Eq. (10)]. In fact, in this case we have that $\langle l_Y \rangle(\mathbf{r}_k, r_2) \gg \langle l_Y \rangle(\mathbf{r}_k, r_1)$, and Eq. (17) has almost the same numerator as Eq. (10) but a smaller denominator. In general, the meaning of Eqs. (16) and (17), at least for DC and AC data types, is clear: all the detectors located at distances less than $\langle \overrightarrow{r} \rangle$ give a negative contribution to the sensitivity, while all the detectors located at distances larger than $\langle \overrightarrow{r} \rangle$ give a positive contribution to the sensitivity. The reason for this property is that the partial and total path lengths of these two data types are always positive, as discussed in Section 2.A. Which contribution prevails, or whether they compensate for each other, depends on the location and size of the region where a change in absorption occurs. For layered changes in the absorption coefficient, we will show that the two contributions compensate for each other for a superficial layer location, yielding an almost

null sensitivity. On the contrary, the contributions add up to be positive and bigger than the sensitivity of the corresponding data type for a deeper location of the layer.

To correct, at least partially, for the drawback of negative sensitivities in the single-slope method, we propose to use a special source-detector arrangement (typically but not necessarily symmetrical) that was previously proposed for a self-calibrating measurement of optical properties in a homogeneous medium [15]. With this special source-detector array, which is described in Section 2.D, we can measure two matched single slopes and take their average. We refer to this approach as a dual-slope method. Finally, we note again that also the equations of this section are general, regardless of the geometry of the medium and heterogeneity of the optical properties. The only assumption we made (beside the validity of first-order perturbation of the DE) is that functions $y(r)$ are linear. In a practical situation, the equivalent absorption changes are found by inverting Eq. (14), which requires the knowledge of total path lengths, as already discussed in the previous section.

C.   Spatial Sensitivity to Focal Changes in Oxy- and Deoxyhemoglobin Concentrations

By reframing the changes of a data type (or its slope) to focal absorption perturbations with generalized path lengths, it is easy to define the sensitivities to focal changes in chromophore concentrations. In the case of NIRS of blood-perfused tissue, oxy- and deoxyhemoglobin are the dominant chromophores. Following the procedure described in previous works [34,35], Eqs. (9) and (15) can be written for two wavelengths (λ_1 and λ_2), and then we obtain two new equations that relate equivalent homogeneous changes in oxy- and deoxyhemoglobin (O and D, respectively) concentrations to their true focal changes. More precisely, the left sides of the new equations contain a linear combination of O_Y and D_Y (or O_{SSlY} and D_{SSlY}), i.e., the equivalent changes of oxy- and deoxyhemoglobin for the Y data type (or the slope of the Y data type), and the right sides contain a linear combination of the true focal hemoglobin changes (O_k and D_k). We can prove that if $S_Y(\lambda_1) \approx S_Y(\lambda_2)$ (for raw data Y) and $S_{SSlY}(\lambda_1) \approx S_{SSlY}(\lambda_2)$ (for the slopes of data Y), Eqs. (10) and (16) also represent with good approximation the sensitivity for a single focal change in hemoglobin concentration at $\mathbf{r}_k$ (O_k or D_k) estimated with data type Y or its slope, respectively. In other words, we claim that $S_Y \approx O_Y/O_k \approx D_Y/D_k$, and $S_{SSlY} \approx O_{SSlY}/O_k \approx D_{SSlY}/D_k$. We observe that the condition of the similarity of the absorption sensitivities at two wavelengths for Eq. (10) or Eq. (16) implies that the crosstalk between the equivalent hemoglobin species (O_Y and D_Y or O_{SSlY} and D_{SSlY}) is negligible.

D.   Dual-Slope Method

In this work, we propose a dual-slope method that considers the average of two matched slopes obtained with a specially configured array of sources and detectors. The requirements of the array configuration are similar to those previously proposed for the self-calibrating measurement of the optical properties of a homogeneous medium, which features insensitivity to source and detector drifts, and to changes in opto-mechanical coupling between probe and tissue [15]. Here, rather than considering absolute measurements of optical properties, we explore the benefits of the dual-slope method to enhance the optical sensitivity to deeper tissue regions. These dual slopes offer some key advantages with respect to standard single-source or single-detector multi-distance methods used in NIRS

[28]; namely, they are less sensitive to localized superficial tissue inhomogeneities, and they feature a localized sensitivity to a deep tissue volume, as opposed to the typical banana shape of NIRS regions of sensitivity.

One possible configuration is a symmetrical source-detector array, like the one previously proposed for the self-calibration method [15], which comprises two sources (S_1 and S_2) and two detectors (A and B), where the distance between S_1 and A is equal to the distance between S_2 and B (short distance), and the distance between S_1 and B is equal to the distance between S_2 and A (long distance). However, we observe that what needs to be equal is the difference between the long and short distances associated with each source. This configuration may be realized in a linear array [as shown in Fig. 1 (top panel)] or in a two-dimensional (2D) array with the sources and the detectors on the vertices of a rectangle. Alternatively, one may use two sources and multiple detectors (A–G) that feature the same set of source-detector separations as the two sources [as shown in Fig. 1 (bottom panel)]. Even in this case, the conditions for applying the dual-slope method are less strict, and source S2 can be moved closer or farther to detector G (Fig. 1). In either case, the idea is to collect two matched slopes, for which the role of each source (and each detector) is switched, i.e., any given source (or detector) that generates data at a short(er) distance for one slope simultaneously generates data at a long(er) distance for the other slope.

The formulas we present here are developed for a source-detector arrangement comprising two sources and several detectors placed such that their distances from the two sources are pair-wise symmetric with respect to the average source-detector distance $\langle \vec{r} \rangle$. Here, we derive the formulas for the DC slope, but the same procedure can be used for the AC and phase slopes. If we apply the DC single-slope method (where $y = \ln[r^2 DC(r)]$ according to the previous section) for source S_1 (Fig. 1), we have

$$SSl_{DC1} = \frac{\overrightarrow{(\vec{r} - \langle \vec{r} \rangle)} \overrightarrow{\ln(r^2 DC_1(r))}}{N \text{var}(\vec{r})} = \frac{\sum_{i=1}^{N} (r_i - \langle \vec{r} \rangle) \ln(r_i^2 DC_1(r_i))}{N \text{var}(\vec{r})},$$ (18)

where SSl_{DC1} is the DC single slope calculated with respect to source S_1 and N is the number of detectors. The formulas can be derived for either even N or odd N. However, we note that for odd N, one of the detectors is placed at $\langle \vec{r} \rangle$ [it is the one at $\langle \vec{r} \rangle = 20$ mm in Fig. 1 (bottom panel)]. This detector does not contribute to the slope values or to its changes in time; therefore, here we derive the formula for even N, in which case we have $r_{N-k} - \langle r \rangle = -[r_{k+1} - \langle r \rangle]$ with $k = 0, 1, \ldots, N/2 - 1$. By using the properties of logarithms, Eq. (18) becomes

$$SSl_{DC1} = \frac{\sum_{k=0}^{N/2-1} (r_{N-k} - \langle \vec{r} \rangle) \left\{ 2\ln\left(\frac{r_{N-k}}{r_{k+1}}\right) + \ln\left(\frac{DC_1(r_{N-k})}{DC_1(r_{k+1})}\right) \right\}}{N \text{var}(\vec{r})}.$$ (19)

Similarly, if we consider the source S_2, we have

$$SSl_{\text{DC2}} = \frac{\sum_{k=0}^{N/2-1}(r'_{N-k}-\langle\overrightarrow{r}'\rangle)\left\{2\ln\left(\frac{r'_{N-k}}{r'_{k+1}}\right)+\ln\left(\frac{\text{DC2}(r'_{N-k})}{\text{DC2}(r'_{k+1})}\right)\right\}}{N\text{var}(\overrightarrow{r}')}.$$ (20)

In Eq. (20), the prime indicates distances calculated with respect to source S_2. In Fig. 1 it is assumed that $r_k = r'_k$, which means, for example, that the distance between S_1 and detector B is the same as the distance between S_2 and detector F. However, this is not strictly necessary for the validity of the dual-slope method, which can be applied under more general conditions. By using the same arguments as in the original work on the self-calibrated method for absolute measurements [15], we note that in a real experiment, the measured DC signal from source S_1 includes contributions related to source emission, detector response, and probe-to-tissue coupling as follows:

$$\text{DC}_1(r_{N-k}) = P_1 C_1 Z(r_{N-k}) C_Z(r_{N-k}) \text{dc}_1(r_{N-k}),$$ (21)

$$\text{DC}_1(r_{k+1}) = P_1 C_1 Z(r_{k+1}) C_Z(r_{k+1}) \text{dc}_1(r_{k+1}),$$ (22)

where P_1 is the power emitted by source S_1, C_1 is the optical coupling factor between source S_1 and the tissue, $Z(r_{N-k})$ [$Z(r_{k+1})$] is the sensitivity of detector Z at r_{N-k} [r_{k+1}], $C_Z(r_{N-k})$ [$C_Z(r_{k+1})$] is the optical coupling factor between detector Z at r_{N-k} [r_{k+1}] and the tissue, and $\text{dc}_1(r_{N-k})$ and $\text{dc}_1(r_{k+1})$ are the theoretical values of DC intensities at a longer (r_{N-k}) and shorter (r_{k+1}) distances. The factors C_1, Z, and C_Z account for random or systematic temporal fluctuations, drifts in source or detector characteristics, displacement of the optical probe, etc., whereas dc_1 does not include any kind of noise or experimental confounds. Similarly, we can write the following for source S_2:

$$\text{DC}_2(r'_{N-k}) = P_2 C_2 Z'(r'_{N-k}) C'_{Z'}(r'_{N-k}) \text{dc}_2(r'_{N-k}),$$ (23)

$$\text{DC}_2(r'_{k+1}) = P_2 C_2 Z'(r'_{k+1}) C'_{Z'}(r'_{k+1}) \text{dc}_2(r'_{k+1}).$$ (24)

Because of the symmetrical source-detector arrangement, we can rewrite Eqs. (23) and (24) as

$$\text{DC}_2(r'_{N-k}) = P_2 C_2 Z(r_{k+1}) C_Z(r_{k+1}) \text{dc}_2(r'_{N-k}),$$ (25)

$$\text{DC}_2(r'_{k+1}) = P_2 C_2 Z(r_{N-k}) C_Z(r_{N-k}) \text{dc}_2(r'_{k+1}),$$ (26)

If we take the average of the single slopes SSl_{DC1} and SSl_{DC2} and substitute Eqs. (21) and (22) in Eq. (19) and Eqs. (25) and (26) in Eq. (20), all the terms affected by temporal fluctuations will cancel out, and we are left with

$$
\begin{aligned}
&\frac{SSl_{\text{DC1}} + SSl_{\text{DC2}}}{2}\\
&= \frac{\sum_{k=0}^{N/2-1} (r_{N-k} - \langle \vec{r} \rangle) \left\{ 2\ln\left(\frac{r_{N-k}}{r_{k+1}}\right) + \frac{1}{2}\ln\left(\frac{\text{dc1}(r_{N-k})}{\text{dc1}(r_{k+1})} \frac{\text{dc2}(r'_{N-k})}{\text{dc2}(r'_{k+1})}\right) \right\}}{N\text{var}(\vec{r})},
\end{aligned}
\tag{27}
$$

where we have used the assumption that $r_k = r'_k$, but no assumption is made on the homogeneity of the medium. We note that Eq. (27) defines an average "true" slope, which depends only on the distribution of the optical properties in the medium (and the position of the source and the detectors), and that is not affected by any instrumental characteristics (laser power, detector sensitivity, coupling). For the case of a homogeneous semi-infinite medium, Eq. (27) defines the true slope that in principle could be calculated by using only a single source and N detectors under ideal conditions (i.e., same detector sensitivities, same detector coupling). Under general conditions we define the dual slope as the average of the slopes obtained from S_1 and S_2 as

$$
DSl_{\text{DC}} = \frac{SSl_{\text{DC1}} + SSl_{\text{DC2}}}{2}.
\tag{28}
$$

Similarly, the dual slopes of AC and phase are respectively defined as

$$
DSl_{\text{AC}} = \frac{SSl_{\text{AC1}} + SSl_{\text{AC2}}}{2},
\tag{29}
$$

$$
DSl_{\varphi} = \frac{SSl_{\varphi 1} + SSl_{\varphi 2}}{2}.
\tag{30}
$$

The sensitivity associated with the dual-slope method is

$$
S_{DSl_Y} = \frac{S_{SSl_{Y1}} + S_{SSl_{Y2}}}{2},
\tag{31}
$$

where $S_{SSl_{Yi}}$ is the sensitivity associated with the single slope calculated with respect to source "i" [Eq. (16)]. Equation (31) implies also that the equivalent absorption change derived with the dual-slope method is the average of the equivalent absorption changes obtained with the two single slopes [Eq. (15)]. We stress again that with these source-detector arrangements, not only do we achieve a signal that is not affected by source power, detector sensitivity, and optical coupling fluctuations, but we also partially correct for the negative sensitivity of single slopes present in some regions of the diffusive medium as pointed out in Section 2.B. In fact, if we consider a focal region close to the medium boundary and located in between source S_1 and detector A [Fig. 1 (top panel)], this region has a negative sensitivity with respect to the single slope calculated by using S_1 and detectors A and B but a positive sensitivity with respect to the symmetric single slope, which uses source S_2 and the same two detectors. By averaging the two single slopes according to the dual-slope method, we achieve a partial compensation of the negative sensitivity. Finally, we note that the dual slope can be defined under more general conditions: in particular, it is

not required that $r_k = r'_k$ but only that $r_k - \langle \vec{r} \rangle = r'_k - \langle \vec{r}' \rangle$ in other words, source S_2 can be moved closer to or farther from detector G [Fig. 1 (bottom panel)].

E. Solution of the Diffusion Equation in the Semi-Infinite Geometry Considered in This Work

We have studied the sensitivity of the raw data at a single source-detector separation [Eq. (10)] and the slope of the raw data [Eq. (16)], the latter for both single-slope and dual-slope methods, for a semi-infinite medium geometry (Fig. 1). For the single-distance data, we have reported only the sensitivity at the farthest distance. In this geometry, the calculations of the partial path lengths [Eq. (5)] are based on the following expression:

$$\tilde{\phi}(\mathbf{r}_s, \mathbf{r}_k, \omega) = \frac{1}{4\pi D}\left[\frac{e^{-\widetilde{\mu_{\text{eff}}}r1}}{r1} - \frac{e^{-\widetilde{\mu_{\text{eff}}}r2}}{r2}\right], \tag{32}$$

which is the solution of the FD diffusion equation with an extrapolated boundary condition for the fluence. The solution is calculated for a point-like source located at $\mathbf{r}_s = (x_0, 0, 0)$ (where $x_0 = 1/\mu'_s$; μ'_s is the reduced scattering coefficient) and calculated at point $\mathbf{r}_k = (x_k, y_k, z_k)$ inside the diffusive medium. The extrapolated boundary is located at $x_b = -2AD$, where A is a parameter that considers the refractive index mismatch between diffusive medium and the outer medium [36], and D is the diffusion factor ($D = 1/(3\mu'_s)$). By the method of images for solving partial differential equations, the virtual source is located at $\mathbf{r}'_s = (-x_0 + 2x_b, 0, 0)$, and therefore $r_1 = |\mathbf{r}_k - \mathbf{r}_s|$ and $r_2 = |\mathbf{r}_k - \mathbf{r}'_s|$. The complex effective coefficient $\widetilde{\mu_{\text{eff}}}$ is $\widetilde{\mu_{\text{eff}}} = \sqrt{\frac{\mu_a}{D} - i\frac{\omega}{vD}}$. By applying Fick's law to Eq. (32) [37,38], we can obtain the complex reflectance (the output complex intensity at $\mathbf{r}_d$ when photons are emitted from $\mathbf{r}_s$) as

$$\widetilde{R}(\mathbf{r}_s, \mathbf{r}_d, \omega) = \frac{1}{4\pi}\left[x_0\left(\frac{1}{r_1} + \widetilde{\mu_{\text{eff}}}\right)\frac{e^{-\widetilde{\mu_{\text{eff}}}r1}}{r_1^2} + (x_0 - 2x_b)\left(\frac{1}{r_2} + \widetilde{\mu_{\text{eff}}}\right)\frac{e^{-\widetilde{\mu_{\text{eff}}}r2}}{r_2^2}\right], \tag{33}$$

where, in this case, $r_1 = |\mathbf{r}_d - \mathbf{r}_s|$, $r_2 = |\mathbf{r}_d - \mathbf{r}'_s|$. As for $\widetilde{R}(\mathbf{r}_k, \mathbf{r}_d, \omega)$, Eq. (33) is used with x_k replacing x_0 and $r_1 = |\mathbf{r}_d - \mathbf{r}_k|$, $r_2 = |\mathbf{r}_d - \mathbf{r}'_s|$. In fact, for this case, the real and virtual sources are $\mathbf{r}_k$ and $\mathbf{r}'_k = (-x_k + 2x_b, 0, 0)$, respectively. The complex total path length $\langle \widetilde{L} \rangle(\mathbf{r}_d, \omega)$ is calculated as

$$\langle \widetilde{L} \rangle(\mathbf{r}_s, \mathbf{r}_d, \omega) = \frac{1}{8\pi D\widetilde{R}(\mathbf{r}_s, \mathbf{r}_d, \omega)}\left[\left(\frac{x_0}{r_1}\right)e^{-\widetilde{\mu_{\text{eff}}}r1} + \left(\frac{x_0 - 2x_b}{r_2}\right)e^{-\widetilde{\mu_{\text{eff}}}r2}\right], \tag{34}$$

where r_1 and r_2 have the same meaning as in Eq. (33). We note that Eqs. (32)–(34) are valid for all the data types in FD and reduce to the DC expressions when $\omega = 0$. The calculations of the mean partial path lengths were carried out by numerical integration by dividing a region into smaller voxels of 1 mm^3 volume. All our FD results were obtained at a modulation frequency $f = 140$ MHz ($\omega = 2\pi f$). The geometrical arrangement of sources and detectors is illustrated in Fig. 1.

F. Considerations on Noise-to-Signal Ratio (NSR)

So far, we have derived theoretical results without considering the noise affecting different data types and the associated slopes. In this section we are going to take noise into account. We define the noise-to-signal ratio (NSR) for data type Y as $\Delta \bar{Y}_{\text{noise}}$. For DC data, $\Delta \bar{Y}_{\text{noise}} = \frac{\sigma_{\text{DC}}}{\text{DC}}$, where σ_{DC} is the standard deviation and DC is the average of DC data calculated in a given time interval (a similar formula applies for AC). For phase data $\Delta \bar{Y}_{\text{noise}} = \sigma_{\text{Ph}}$, where σ_{Ph} is the standard deviation of phase. Typical values of $\frac{\sigma_{\text{DC}}}{\text{DC}}$, $\frac{\sigma_{\text{AC}}}{\text{AC}}$, and σ_{Ph} are 0.1%, 0.1%, and 0.1°, respectively. For the single slope, where only two distances are used (r_1, r_2; $r_2 > r_1$), we remind that the changes in slope are given by

$$\Delta SSl_Y = \frac{\Delta \bar{Y}(r_2) - \Delta \bar{Y}(r_1)}{r_2 - r_1}. \tag{35}$$

By the formula of *a priori* error propagation, we obtain the following result for the noise level of a slope change:

$$\Delta SSl_{Y\_\text{noise}} \times (r_2 - r_1) = 2\Delta \bar{Y}_{\text{noise}}, \tag{36}$$

where $\Delta SSl_{Y\_\text{noise}}$ indicates the noise level of slope change for data type Y, and where we assumed equal noise level at the two source-detector separations. By analyzing phantom data (not shown), we have found that a better representation of the error in the slopes is obtained by adding the errors of the raw data at the two distances quadratically to yield (for the case of equal NSR at both distances)

$$\Delta SSl_{Y\_\text{noise}} \times (r_2 - r_1) = \sqrt{2}\Delta \bar{Y}_{\text{noise}}. \tag{37}$$

We note that Eq. (37) is correct only if the raw data do not contain relevant drifts; otherwise, the error propagation will yield an overestimate of the errors in the slopes. The same is true for the error in the dual-slope method: adding the errors in the single slopes quadratically yields the correct representation of the error in the dual slope only if any relevant drift is absent in the two slopes. Making this assumption, and assuming equal errors in the two slopes, we have that

$$\Delta DSl_{Y\_\text{noise}} \times (r_2 - r_1) = \Delta \bar{Y}_{\text{noise}}, \tag{38}$$

where $\Delta DSl_{Y\_\text{noise}}$ is the noise level of dual-slope change for data type Y. By using the relationship between change in data type (due to a focal change in absorption at $\mathbf{r}_k$, $\Delta \mu_a$) and the corresponding partial path lengths, we have a useful way to determine a limit of detectability in simulated data (i.e., when the source of contrast is equal to the noise level). For the single-distance data Y, we have

$$\Delta \bar{Y}_{\text{noise}} = \left| \langle l_Y \rangle (\mathbf{r}_k, r) \Delta \mu_a \right|, \tag{39}$$

where the left side is equal to 0.1% for DC or AC data and $1.7 \cdot 10^{-3}$ rad (0.1°) for phase data. For the single-slope method, we have

$$\Delta SSl_{Y\_\text{noise}} \times (r_2 - r_1) = \left| [\langle l_Y \rangle (\mathbf{r}_k, r_2) - \langle l_Y \rangle (\mathbf{r}_k, r_1)] \Delta \mu_a \right|, \tag{40}$$

where $\langle l_Y \rangle (\mathbf{r}_k, r_i)$ is the path length spent by detected photons (at the source-detector separation r_i) inside the focal region at $\mathbf{r}_k$. The left side is equal to $\sqrt{2} \cdot 0.1\%$ for DC and AC data and $\sqrt{2} \cdot 1.7 \cdot 10^{-3}$ rad for phase data. For the dual-slope method, we have that

$$\Delta DSl_{Y\_\text{noise}} \times (r_2 - r_1) = \frac{1}{2} \left| \{ [\langle l_Y \rangle_{S_1}(\mathbf{r}_k, r_2) + \langle l_Y \rangle_{S_2}(\mathbf{r}_k, r_2)] - [\langle l_Y \rangle_{S_1}(\mathbf{r}_k, r_1) \\ + \langle l_Y \rangle_{S_2}(\mathbf{r}_k, r_1)] \} \Delta \mu_a \right|, \tag{41}$$

where $\langle l_Y \rangle_{S_j}(\mathbf{r}_k, r_i)$ indicate the partial pathlength (for data type Y) inside the focal defect at $\mathbf{r}_k$ when photons are detected at a source-detector separation r_i calculated from source S_j (Fig. 1). The left-hand side is equal to 0.1% for DC or AC data and ~0.0017 rad (0.1°) for phase data. We note that in Eqs. (39)–(41) the right-hand sides are known from the simulations, and they are the absolute values of the source of contrast. The limits of detectability are defined when the source of contrast is equal to the noise level [left side of Eqs. (39)–(41)]. By using Eqs. (10) and (16) we can also determine the noise level of the equivalent absorption change and the noise level of oxy- and deoxyhemoglobin oscillations. We note that the noise level of equivalent absorption change is wavelength dependent, and therefore in a given scenario where oxy- and deoxyhemoglobin oscillations are associated with different tissue regions, it is possible that only the equivalent absorption change at one wavelength is above noise level. This may happen in situations when the NSR ~ 1. In this case, nothing can be concluded about the equivalent oxy- and deoxyhemoglobin changes derived with the method proposed (i.e., if they are below or above noise level), unless we propagate the errors to determine their noise levels. In the following discussions we have applied Eqs. (39)–(41) to determine the noise level for the change of data type (or the change of its slope) in the numerical results.

3. RESULTS

The results are presented in four sections: one for layered absorption changes (Section 3.A), two for focal absorption changes (Sections 3.B and 3.C), and one where we apply the NSR considerations to numerical results (Section 3.D). Both layered and focal changes are of interest for describing hemodynamics that are usually studied in functional near-infrared spectroscopy (fNIRS) of the human head. When one studies cerebral hemodynamics of systemic origin {like in coherent hemodynamics spectroscopy (CHS) [26]}, layered absorption changes may likely be a good approximation. For typical cases of brain activation [27], the hemodynamic changes are usually more complex, with focal changes occurring in the brain cortex and hemodynamic confounds occurring in the extracerebral tissue layers (scalp, skull, etc.). In each case, we show the sensitivity of single-distance data [Eq. (10)], single-slope data [Eq. (16)], and dual-slope data [Eq. (31)]. For the single-distance data, we will always refer to the farthest distance considered here (35 mm).

We also studied the performance of the different methods to recover periodic oscillations in oxy- and deoxyhemoglobin, which are described by the phasors $\mathbf{O}$ and $\mathbf{D}$, respectively [26]. This part will be in Section 3.A for layered changes and in Section 3.C for focal changes. In

particular, in CHS we are interested in measuring **D/O**, i.e., the ratio of amplitudes and the phase difference between the two hemoglobin species. For the simulations, we have assigned two (true) phasors for **O** and **D** (**O**$_T$ and **D**$_T$) to each region of the medium where oscillations occurred. We translated **O**$_T$ and **D**$_T$ phasors into (true) absorption phasors at two wavelengths (690 and 830 nm). We recovered the phasors corresponding to the equivalent absorption change for the single-distance data, for the single slope and dual slope by using Eqs. (9), (15), and the equation derived from Eq. (31), respectively. The recovered phasors of absorption oscillations were translated into estimated phasors for oxy- and deoxyhemoglobin **O**$_E$ and **D**$_E$. Finally, we compared **D**$_T$/**O**$_T$ (defined for each region) with **D**$_E$/**O**$_E$, which is the equivalent phasor ratio obtained for each method. In Section 3.D we revisit the numerical results of the previous three sections by adding a few comments onNSR.

A.   Sensitivity to Layered Absorption Changes

One example of sensitivity for layered changes in the absorption coefficient is shown in Fig. 2, obtained with the source-detector arrangement of Fig. 1 (top panel). The sensitivities were obtained according to Eq. (10) [Fig. 2 (top panel)] or Eq. (16) [Fig. 2 (bottom panel)] by scanning a layer of size $1 \times 80 \times 80$ mm (in the x, y ,and z directions), along the depth of the medium (x axis) with 1 mm increments. The center of the layer was fixed in the (y and z) directions at (20 and 0) mm. The optical properties of the medium were $\mu_a = 0.01$ mm^{-1} and $\mu'_s = 1$ mm^{-1}; the refractive indices of the diffusive medium and outer medium were $n_i = 1.4$ and $n_o = 1$, respectively. The modulation frequency for AC and phase data was 140 MHz. We note that for this case of layered changes, the results of the slope method are the same regardless of which single slope we are considering (with respect to source S$_1$ or S$_2$ of Fig. 1) or ifwe average them according to the dual-slope approach. Therefore, in this case, we will indicate both sensitivities (with single or dual slope) as S_{SIY}. Two important features of Fig. 2 are (1) the shift towards the right (deeper regions of the medium) of the maxima of S_{SIY} with respect to the maxima of S_Y and (2) the almost null sensitivity of S_{SIY} when the layer is close to the medium boundary. This result is because the region of the layer close to detector A (close detector) has a negative sensitivity that is compensated for by the positive sensitivity of the region close to detector B (far detector). The reason why DC and AC do not have the maximum sensitivity when the layer is at $x = 0.5$ mm (top position) is because these data types have a high sensitivity mostly around source and detector but very little in the central region of the layer (this region is crossed mainly by a few photons with short paths). As we scan the layer further down to a depth of 5 mm, the sensitivity to the layer region close to source and detector is smaller, but it is bigger in the central part of the layer (now more photons with longer paths will cross the entire layer), causing an overall increase in sensitivity.

The negligible value of S_{SIY} to absorption changes occurring at shallow depths shows that a slope method offers a natural "depth filter" for cases when hemodynamics oscillations occur both close to the boundary and deeper in the medium. We prove this point by considering two cases of **D/O** estimation. In the first case we consider hemodynamic oscillations, which occur only in two layers at the same time: a top layer 1 mm thick that occupies the region $x \in [0, 1]$ mm and a deeper layer 1 mm thick that occupies the region $x \in [15, 16]$ mm. These

layers are representative of a skin layer (or top layer "T") and a brain layer (or bottom layer "B"). The phasors describing the true oscillations are: $\mathbf{O}_1 = \mathbf{O}_2 = 1e^{i0}$ μM, $\mathbf{D}_1 = 0.4e^{i0}$ μM, and $\mathbf{D}_2 = 0.4e^{i3/4\pi}$ μM. The subscripts "1" and "2" indicate the top layer and bottom layer, respectively. Therefore, we have that $\frac{\mathbf{D}_{1T}}{\mathbf{O}_{1T}} = 0.4e^{i0}$ and $\frac{\mathbf{D}_{2T}}{\mathbf{O}_{2T}} = 0.4e^{i3/4\pi}$. Figure 3 shows the comparison between the estimated ratio of phasors $\mathbf{D}_E/\mathbf{O}_E$ with DC and the DC slope method (left panel) and with phase and the phase slope method (right panel). The true ratio of phasors relative to top and bottom layer $\mathbf{D}_T/\mathbf{D}_T$ are indicated by the labels "T" and "B" (red arrows), respectively. We have not reported the ratio of phasors estimated with AC and the AC slope because they are almost identical to those obtained with DC and the DC slope, respectively. From the left panel we can see that while DC data yields a ratio of phasors "closer" to the true one of the top layer, the DC slope method yields a ratio of phasors very close to the true one in the bottom layer. Phase and the phase slope method yield phasor ratios almost overlapping with the true phasor ratio of the bottom layer. These results were obtained by using a modulation frequency of $f = 140$ MHz and background optical properties of $\mu_s'(690 \text{ nm}) = 1.2$ mm^{-1} and $\mu_s'(830 \text{ nm}) = 1$ mm^{-1}, and the absorption coefficients at the two wavelengths were calculated by considering a total hemoglobin concentration ([HbT]) of 45 μM and a hemoglobin saturation (St) of 0.65. Similar results (not shown) were obtained for $\mu_s'(690 \text{ nm}) = 1.5$ mm^{-1} and $\mu_s'(830 \text{ nm}) = 1.2$ mm^{-1} and for the absorption coefficients at the two wavelengths relative to [HbT] of 75 μM and St of 0.65.

In the second case, we also consider hemodynamic oscillations that occur in two layers at the same time: a top layer 6 mm thick that occupies the region $x \in [0, 6]$ mm (indicated by "T") and a deeper layer 6 mm thick that occupies the region $x \in [12, 18]$ mm (indicated by "B"). The phasors describing the true oscillations (red arrows) are the same as before for the top and bottom layers. The background optical properties and modulation frequency are also the same as those of the previous case. The results are shown in Fig. 4.

The case shown in Fig. 4 may be a closer representation of what happens during induced hemodynamic oscillations in CHS, with systemic oxy- and deoxyhemoglobin changes occurring both in the scalp and in the brain and most likely a region of negligible oscillations in the skull and cerebrospinal fluid (CSF) layers. As before, the ratios of phasors estimated with DC and the DC slope are on the left panel, while those estimated with phase and the phase slope are on the right panel. For this case, except the phasor's ratio estimated with phase slope, which is coincident with the true phasor's ratio of the bottom layer, all the other data types and slopes show a different degree of mixture between the true phasor ratio of the top and bottom layer. The phasor ratio estimated with DC is the closest to the true phasor ratio of the top layer (left panel); this is followed by the one obtained with the DC slope, which points at an angle in between the two true phasor ratios (left panel). The phasor ratio estimated by phase is closer to the true one of the bottom layer (right panel). If we changed the geometry of the two layers or the magnitude of oscillations (by keeping the true phasor ratio fixed), which in the real tissue might be stronger in the brain, we would have that all the phasor ratios estimated by the raw data and the slopes method would rotate counterclockwise toward the true phasor ratio of the bottom layer. We note that we could have obtained similar results if we had directly applied the sensitivity functions Eqs. (10)

and (16) to the ratio of phasors describing oxy- and deoxyhemoglobin oscillations ($\mathbf{O}_E/\mathbf{O}_T$ and $\mathbf{D}_E/\mathbf{D}_T$). For the case of Fig. 3, the discrepancy between the phasors ratio retrieved by using the two methods is less than 5° and less than 9% for the angles and the amplitudes.

B. Sensitivity to Focal Absorption Changes

We now study the sensitivity of the single-distance data and their slopes to focal changes in absorption. We will report only DC and phase data because of the similarity of AC data and derived slopes with those of DC data. By considering the source-detector arrangement of Fig. 1 (top panel), we scan a rectangular cuboid of size $1 \times 5 \times 5$ mm (in the x, y, and z directions, respectively) along the y (horizontal) and x (vertical) directions at 1 mm step increments. The sensitivity maps reported in Fig. 5 were obtained by considering the source-detector pair S_1B in Fig. 1 (top panel) (distance of 35 mm). As expected from Section 2.A, DC always shows a positive sensitivity, while the phase has a more complex behavior. The computations were performed for the optical properties and modulation frequency are the same as those of Fig. 3 and 4 at 690 nm. The white (saturated) pixels in the DC map represent values higher than approximately 4.5×10^{-3}.

Both DC intensity and phase sensitivity maps have the well-known "banana" shape [39,40]. In Fig. 6 we show cross-sectional lines of the map of Fig. 5 at different depths ($x = 0.5, 3.5, 6.5, 9.5, 12.5, 15.5$ mm). Some notable features of Fig. 6 are (a) DC always shows a positive sensitivity, while the phase can have either a positive or negative sensitivity (as described in Section 2.A); (b) with respect to DC, phase data are less sensitive close to the medium boundary and more sensitive in deeper regions of the diffusive medium; and (c) the asymmetric behavior of DC intensity at a depth of $x = 0.5$ mm results from the introduction of an effective source inside the medium, breaking the symmetry of the source-detector configuration. Also, the voxel discretization used for the calculation in this work caused more photons to be "absorbed" when the region was close to the detector than when it was close to the source. The asymmetry is not visible in phase data, because for focal absorption increases in both locations (i.e., close to the source and close to the detector), comparable fractions of short-path and long-path photons were "absorbed," and the phase was affected almost equally. Figure 7 shows the sensitivity maps for single slopes of DC (top panel) and phase (bottom panel). The two sets of saturated pixels represent values less than −0.01 (black) and higher than 0.02 (white). They were obtained by using the source-detector pairs S_1A and S_1B [Fig. 1 (top panel)] (distances of 20 and 35 mm). As discussed in Section 2.B, S_{SSI_Y} can be either positive or negative. The locations of a focal region where S_{SSI_Y} becomes negative are in proximity of the detector at the shortest distance from the source (detector A, which is 20 mm from S_1). Even though the slope method features a greater sensitivity to deeper tissue regions with respect to single-distance data, the areas of negative sensitivity can be problematic for the interpretation of the data. Figure 8 represents some cross-sectional lines of the sensitivity maps of Fig. 7 for single slopes, where each plot refers to a different depth. From Fig. 8 we note that the phase slope has a smaller sensitivity than the DC slope at shallow depths ($x = 0.5$ and 3.5 mm) but a greater sensitivity in deeper regions of the tissue ($x > 12.5$ mm). All the single slopes show positive as well as negative sensitivities, especially for absorption changes close to detector A. For DC, the single-slope sensitivity is very large and negative in proximity of detector A (close detector) and very

large and positive (even greater than for single-distance data) close to detector B (see plot at $x = 0.5$ mm). By comparing the cross-sectional lines in Figs. 6 and 8, we note that deeper in the tissue (for example, $x = 12.5$ and 15.5 mm) the sensitivity of DC and phase single slopes are greater than for the corresponding single-distance data. The dual-slope method compensates, at least partially, for the drawbacks of the single slopes, i.e., the negative sensitivity and the strong positive sensitivity to focal perturbations close to the detectors. For the dual-slope method we use S1A (short distance) and S_1B (long distance) for calculating one slope, and we use S_2B (short distance) S_2A (long distance) for calculating the other slope [Fig. 1 (top panel)]. However, we observe that the result would not change if we were to use S_1A and S_2A for one slope and S_2B and S_1B for the other slope. These two slopes are averaged according to the dual-slope method. The sensitivity maps of DC and phase with the dual-slope method are shown in Fig. 9.

In Fig. 9 the white pixels indicate regions where the sensitivity is higher than approximately 7×10^{-3}. A comparison of Figs. 9 and 7 confirms that the regions of negative sensitivity of the dual slopes feature a reduced sensitivity value with respect to the single slopes. This feature is more obvious when we look at the cross-sections of the sensitivity along the y axis at different depths as shown in Fig. 10 (DC dual slope) and Fig. 11 (phase dual slope). From Fig. 9, one can see that the phase dual slope has more desirable features than the DC intensity dual slope, in that its maximal sensitivity to focal absorption changes is deeper in the tissue (~11 mm versus ~5 mm), and its sensitivity to superficial (~2 mm depth) absorption changes is lower (−0.004 versus −0.0055). A quantitative comparison between the sensitivities obtained with the dual-slope method and those obtained with single-distance data shows that the advantages of the former outweighs its only drawback, which is the presence of some residual negative values close to the medium boundary. When we compare DC dual-slope and single-distance data, we observe that (a) the dual-slope DC has a much more spatially confined region of positive sensitivity than the typical "banana shape" of single-distance DC data (Fig. 5) and (b) the DC dual slope has a higher positive sensitivity than single-distance DC data (except for superficial tissue: $x = 0.5$ mm). Similarly, if we compare the sensitivities obtained with dual-phase slope and single-distance phase data, we see that (a) the dual-phase slope has a much more spatially confined region of positive sensitivity compared with the positive "banana" of the single-distance phase data (Fig. 5); (b) the dual-phase slope has a smaller positive sensitivity than the single-distance phase data down to a depth of $x = 6.5$ mm and a higher sensitivity deeper in the medium; and (c) the region of negative sensitivity is more spatially confined than that of the single-distance phase data, but the values are slightly more negative.

We can further reduce the negative sensitivities present in the dual-slope method if we consider a multi-detector arrangement [Fig. 1 (bottom panel)] as shown in Fig. 12. We note that this arrangement is currently only possible with DC instrumentations that feature a suitably large dynamic range [41]. Of course, one can choose other arrangements that use more than two detectors but require a smaller dynamic range. By comparing Figs. 9 and 12, we note that even though the negative sensitivities are smaller for the configuration featuring seven detectors, the regions of positive sensitivity are also slightly smaller and less spatially confined than those obtained with two detectors.

C. Recovery of Localized Oscillations of Oxy- and Deoxyhemoglobin Concentrations

Let us now consider two examples of phasors ratio retrieval (**D/O**) as it was done for the case of layered absorption changes. These examples reflect situations of periodic brain activation (in response to a block paradigm) where a focal change in cerebral hemodynamics occurs synchronously with hemodynamic changes in the extracerebral tissue layers. The hemodynamic changes in the brain are often larger than in the extracerebral layers. The geometry is shown in Fig. 13. In both cases, we will compare only the results obtained with the single-distance data and with the dual-slope methods because the single-slope methods yielded results that are almost coincident with those of the dual-slope methods. This is true because of the particular focal perturbations used (which involve absorption changes over a superficial layer with a relatively large area in the $y - z$ plane).

In a first case, we consider three top regions (6 mm thick and 22×40 mm in lateral dimensions) that are characterized by the same oscillations of oxy- and deoxyhemoglobin concentrations, expressed by the phasors $\mathbf{O}_1 = \mathbf{O}_2 = \mathbf{O}_3 = 1e^{i0}$ μM, and $\mathbf{D}_1 = \mathbf{D}_2 = \mathbf{D}_3 = 0.4e^{i0}$ μM, which represent a blood volume oscillation. We also consider a deeper region (a cube of 10 mm side) that is characterized by the phasors $\mathbf{O}_4 = 5e^{i0}$ μM and $\mathbf{D}_4 = 5e^{i3/4\pi}$ μM, which represent an almost pure blood flow oscillation (for a pure blood flow oscillation deoxy- and oxyhemoglobin would be shifted by π).

Figure 14 shows the retrieval of the phasor ratio $\mathbf{D}_E/\mathbf{O}_E$ by using single-distance DC and dual-slope DC (left panel) and single-distance phase and dual-slope phase (right panel). In a second case (Fig. 15) we consider different hemodynamics in the top three regions $\mathbf{O}_1 = \mathbf{O}_2 = \mathbf{O}_3 = 1e^{i0}$ μM, $\mathbf{D}_1 = 0.4e^{i0}$ μM, $\mathbf{D}_2 = 0.4e^{i\pi/3}$ μM, and $\mathbf{D}_3 = 0.4e^{i\pi/2}$ μM and in the deeper region $\mathbf{O}_4 = 5e^{i0}$ μM and $\mathbf{D}_4 = 5e^{i3/4\pi}$ μM. As we can see in Figs. 14 and 15, the closest measure of the phasor ratio for the deeper region is obtained with the phase dual-slope method. Specifically, the fractions between the estimated amplitude of the phasor ratio and the true amplitude of the phasor ratio in the deepest region 4 (i.e., $|\mathbf{D}_E/\mathbf{O}_E|/|\mathbf{D}_4/\mathbf{O}_4|$) for the single-distance DC, dual-slope DC, single-distance phase and dual-slope phase, respectively, are ~0.25, ~0.47, ~0.62, and ~1.1,in Fig. 14and ~0.34, ~0.66, ~0.69,and ~1.1 in Fig. 15. The DC dual slope and single-distance phase gave similar results. In both cases, the single-distance DC data always yielded a phasor ratio closer to the one of the three top regions. Note that the amplitudes of the retrieved phasors with the different methods, $\mathbf{O}_E$, $\mathbf{D}_E$, are comparable to values measured in a typical CHS protocol [42].

D. Analysis of Signal-to-Noise Ratio: Application to Numerical Results

In this section, by using the equations describing the NSR [Eqs. (39)–(41)], we revisit the example of Fig. 15 and add a few considerations about the signal-to-noise ratio [SNR(λ), which is the inverse of NSR]. The purpose is twofold: (1) to understand why a retrieved ratio of phasors is in the direction it is found and (2) which region (characterized by certain phasors) in the medium is detectable (i.e., has SNR ≥ 1). This is done for a "typical" case of brain activation with some superficial confound (Fig. 15). For answering the first question, one does not need to use the concept of SNR, it suffices for each region to calculate the source of contrast (right side of Eqs. (39)–(41), i.e., the signal) and compare them. We remind that the source of contrast (or signal) in one region depends on the partial path length

spent by detected photons in that region and by the change in the absorption coefficient. Since we have specified the oscillations of oxy- and deoxyhemoglobin in each region, we can determine the contrast in each region. If the source of contrast in one region is much bigger than the others, the retrieved ratio of phasors will be very close to the true ratio of phasors in that region. If the sources of contrast in different regions are similar, the retrieved ratio of phasors will be pointing in an "intermediate" direction. These considerations apply also if none of the regions are detectable. On the contrary, by dividing the source of contrast by the noise we add the information if a region is detectable or not. Note that several regions may not be detectable separately, but they do when they are combined.

In a final example, we will also report the SNR maps for changes of absorption coefficient derived from localized changes of oxy- and deoxyhemoglobin concentration where both the volume of the region and the changes of hemoglobin concentrations are typical of brain activation. The purpose is to understand which method can be used to detect a focal perturbation in a realistic case of brain activation. We define the SNR as $\mathrm{SNR}_{\bar{Y}}(\lambda) = \Delta\bar{Y}(\lambda) / \Delta\bar{Y}_{\mathrm{noise}}(\lambda)$ for the single-distance data Y, $SNR_{SSI_Y}(\lambda) = \Delta SSI_Y(\lambda)/\Delta SSI_{Y\_\mathrm{noise}}(\lambda)$ for the single slope, and $SNR_{DSI_Y}(\lambda) = \Delta DSI_Y(\lambda)/\Delta DSI_{Y\_\mathrm{noise}}(\lambda)$ for the dual slope. More precisely $\Delta\bar{Y}$, ΔSSI_Y, and ΔDSI_Y (the signal levels) are given by the right-hand sides of Eqs. (39)–(41), respectively, and $\Delta\bar{Y}_{\mathrm{noise}}$, $\Delta SSI_{Y\_\mathrm{noise}}$, and $\Delta DSI_{Y\_\mathrm{noise}}$ (the noise levels) are those discussed in Section 2.F. We recall that in our simulations we have used only two wavelengths, $\lambda_1 = 690$ nm and $\lambda_2 = 830$ nm, and that for each data type Y, the SNR analysis is carried out only at the farthest source-detector separation (and specifically for source S_1 and detector B of Fig. 13). For the single slopes, we have considered only source Si and detectors A and B of Fig. 13. In the example of Fig. 15, different oscillations of oxy- and deoxyhemoglobin concentrations were assigned to different focal regions of the medium and assumed to be present at the same time. Even in this case, our proposed method always retrieves one equivalent oscillation for oxy- and deoxyhemoglobin (for each single-distance data type or associated single-slope or dual-slope case), which is the result of the combined effect of all the concentration oscillations in the medium. However, by calculating the right-hand sides of Eqs. (39) and (41) (which represent the signal level) separately in each region where oscillations occur, we can calculate their SNR, which tells us how closely the retrieved equivalent oscillations will reproduce the real ones in each region.

The SNR results for the example of Fig. 15 are reported in Table 1 for single-distance and dual-slope data (for both DC intensity and phase) associated with absorption changes in regions 1, 2, 3, and 4 (4 being the cubic region). With single-distance and dual-slope phase data, only the cubic region 4 yielded a SNR above the noise level. With the single-distance phase, we have that $\mathrm{SNR}_\varphi(\lambda_1) = 3.5$ and $\mathrm{SNR}_\varphi(\lambda_2) = 1.3$; however, these two SNR_φ account for 77% and 56% of the total SNR_φ at λ_1 and λ_2, respectively. In fact, even if no other region yielded a SNR above noise when considered individually, the combined effect of regions 1, 2, 3 did. For these reasons, the retrieved phasors ratio with single-distance phase is not exactly coincident with the true phasors ratio of the cubic region. With dual-phase slope we have $\mathrm{SNR}_{DSI_\varphi}(\lambda_1) = 3.3$, $\mathrm{SNR}_{DSI_\varphi}(\lambda_2) = 1.2$, which account for 95% and 91% of the total SNR, respectively. Therefore, the phasor ratio obtained with dual-phase slope

should be the closest to the true one of the cubic region as shown in Fig. 15. These numbers give some indication about the retrieved phasor ratio with the different methods. For example, for DC single-distance data, regions 1, 2, and 4 contribute almost equally to the total SNR at λ_1 (33%, 32%, and 35%, respectively), while at λ_2 the SNR originates mostly from regions 1 and 2 (41% and 40%, respectively) and less from region 4 (18%). For the DC dual slope, region 1 has a small contribution to the total SNR (4% at λ_1). Slightly bigger contributions with respect to DC data come from region 2 (34% and 54% at λ_1 and λ_2, respectively). The largest increase of SNR with respect to DC single-distance data achieved with DC dual slope is found in the cubic region (59% and 37% at λ_1 and λ_2, respectively). These considerations are consistent with a ratio of phasor retrieved with DC dual slope, which is closer to the true ratio of phasors of the cubic region than that obtained with DC single-distance data (Fig. 15). Similar reasoning applies also for phase single-distance and phase dual-slope data (Fig. 15), as discussed above.

Finally, we want to study the SNR for the case of a "realistic" brain activation. As reported [27] during visual stimulation, a local increase of about 30% in cerebral blood volume has been measured. We model a focal brain activation as a cuboid of sides $2 \times 10 \times 10$ mm in the *x, y*, and *z* directions, where 2 mm is representative of the thickness of the brain cortex. The cuboid was scanned in a semi-infinite medium geometry with 1 mm step in both the *x* and *y* directions. We used the background optical properties of Fig. 3 (at $\lambda_1 = 690$ nm) and for the perturbation we increased [HbO] by 9 μM and [Hb] by 5 μM [which caused $\Delta\mu_a(\lambda_1) = 0.0033$ mm^{-1}], in this way we kept hemoglobin saturation (St) fixed at 0.65. To be consistent with the sensitivity maps [Figs. 5, 7, and 9] we used Eqs. (39)–(41) with the right terms without absolute value and with a minus sign preceding them. In this way we can define a SNR with a sign, with the properties that its absolute value represents the true SNR (positive by definition), and its sign is the same of the equivalent absorption change. The maps of SNR are reported for DC, DC single slope, and DC dual slope (Fig. 16) and for phase, phase single slope, and phase dual slope (Fig. 17). Looking at Figs. 16 and 17 we can highlight the following points: (1) in general DC data (single distance, single slope, dual slope) are characterized by a much higher SNR at all depths than phase data; (2) in particular, while DC single-distance data shows the highest SNR at all depths, it is the highest in the top 4–5 mm and especially in regions close to the source and the detector {saturated white pixels in [Fig. 16 (top panel)]}, which makes this data type particularly sensitive to superficial changes in absorption; (3) the DC single slope has a smaller and more spatially localized SNR compared to single-distance DC data, but it also features a region of negative SNR (reflecting the negative sensitivity) close to the detector at the shorter distance [Fig. 16 (middle panel)]; (4) the signal obtained with DC dual slope has the most spatially confined positive SNR [Fig. 16 (bottom panel)], and the regions with negative SNR have smaller values when compared with single slope, and this is due to the partial cancellation of the negative sensitivities intrinsic in the dual-slope method; (5) phase data shows a "banana-shaped" region of positive SNR (above noise level) with rather constant values down to depths of 12–13 mm. There is also a central top region (between source S_1 and the farthest detector) of negative SNR, which is below the noise level, showing that phase data are not sensitive to absorption changes occurring close to the medium boundaries; (6) the phase dual slope has the most desirable features for imaging. In fact, not only does it show a negative

SNR below noise in the top 6–7 mm, it also shows a very confined region of positive SNR that spans the depths ~8 – 15 mm and about 10–15 mm width. The only drawback is the low SNR.

Similar results were also found for different background properties characterized by [HbT] of 75 μM, St of 0.65, $\mu_s'(\lambda_1) = 1.5$ mm^{-1}, and $\mu_s'(\lambda_2) = 1.2$ mm^{-1}. In this case the 30% increase in [HbT] (by keeping a constant St) was obtained by increasing the oxy- and deoxyhemoglobin concentrations at the defect by 15 μM and 8 μM, respectively, relative to background values.

4. DISCUSSION

In this work, we have shown through diffusion theory that dual slopes based on DC intensity, AC amplitude, or phase data types achieve a greater relative sensitivity to deep versus shallow regions in a diffusive medium with respect to single slopes. Compared to single-distance and single-slope data, the dual-slope method also features a more spatially confined region of sensitivity that does not extend to the medium surface (as it is the case for banana-shaped regions of sensitivity) and reaches more deeply into the medium when phase rather than intensity data are used. We have used the concept of equivalent absorption change, which is defined as the homogeneous change in the absorption coefficient of the whole medium that yields the same data type change (or change in the slope of a data type) that is measured when one or more focal absorption changes are present in the medium. The definition of equivalent absorption change for each data type (and derived single and dual slopes) uses generalized path lengths introduced in our previous work [30]. This method is general and applies to any geometry of diffusive medium and any distribution of the optical properties within the medium. Also, it has the advantage of not mixing data types with different features of spatial sensitivity. The sensitivity is defined for a single focal absorption change as the ratio of the equivalent absorption change to the true focal change. Equivalent absorption changes to focal absorption perturbations calculated with single slope feature regions of negative sensitivities, particularly close to the short-distance detector when the single slopes are calculated by using one source and two detectors. The dual-slope method by using a symmetric source-detector arrangement also achieves a partial correction and cancellation of the negative sensitivity. This arrangement was proposed in the literature for the so-called "self-calibrating" approach to absolute estimation of the optical properties, by which it is possible to measure absolute optical properties of a diffusive medium without previous calibration. The self-calibrating method features high insensitivity to light source power and detector sensitivity fluctuations as well high insensitivity to changes in the coupling between the input source and the probed medium as well as the medium and the detectors (usually trough optical fibers). The self-calibrating approach has also been used in several studies for measuring dynamic changes of oxy-, deoxyhemoglobin, and oxygen saturation. In these studies, it was also assumed that the changes in DC slope originated from homogeneous changes in the absorption coefficient. In the present work, we moved away from such homogeneity assumption and provided a rigorous and general framework for this approach (not restricted to DC data only) to sense tissue heterogeneities, which in principle could be extended toward the inverse imaging problem [see, for example, Eq. (13),

which correlates the change in slopes and the focal changes in the absorption coefficient]. We have used source-detector arrangements similar to those proposed in the literature, and we have shown their imaging capabilities through sensitivity maps, at the same time retaining the benefits in terms of stability of the signals of the self-calibrating method.

For the single-distance data, we have shown that the sensitivity of DC is higher than that of the phase at shallow depths, while the opposite is true deeper in the medium. This is the case for single-distance, single-slope, and dual-slope data. However, we point out that DC data are characterized by a much greater SNR than the phase data. Therefore, even though phase dual-slope has some of the most desirable features for imaging purposes, due to its low SNR it may not be always applicable to experimental data, depending on the nature (absorption contrast, size, and duration) of the target optical contrast. In this case, one can use the DC dual-slope method, which features a higher SNR and a better ratio of sensitivities between deep and shallow regions than DC single-distance data.

The dual-slope method requires a minimum of two sources and two detectors, and we have made the case, contrary to a large portion of the literature, that we do not necessarily need a "short" source-detector separation to suppress extracerebral hemodynamic contributions to signals collected at "large" source-detector distances, since the dual-slope method (especially with phase data) is intrinsically weakly sensitive to localized changes close to the surface. However, we note that we can apply the dual-slope method also with multiple source-detectors [Fig. 1 (bottom panel)] and therefore benefit also from the information of several single-distance data.

Through theoretical results, we have made a case that dual-phase slope, despite the low SNR, can be used for typical scenarios of NIRS. In particular, we have focused on the retrieval of the ratio of oxy- and deoxyhemoglobin oscillations in a typical protocol used in CHS, which is a novel method to obtain information on cerebral microvascular integrity and autoregulation. We have also retrieved the ratio of oxy- and deoxyhemoglobin oscillations in a typical case of periodic brain activation. In both cases, the dual-slope methods (particularly with phase data) yielded a ratio of hemoglobin oscillations very close to the true one in the brain. However, we stress that the dual-slope method could be used in other applications of NIRS as a simpler alternative to more complex methods typical of diffuse optical tomography. In a complementary work, we show that the dual-slope method can be successfully applied to experimental data from the human head during a typical protocol of coherent hemodynamic spectroscopy, and the *in vivo* results are consistent with the claims of this work [43].

Finally, we observe that a common multi-distance formula used in the semi-infinite medium geometry [28] uses both AC and phase slope to retrieve the absolute value of the absorption and the reduced scattering coefficients. The formula for the retrieval of the absorption coefficient can also be used for estimating equivalent absorption changes due to arbitrary focal changes in the medium. However, both phase slope and AC slope changes will contribute to the absorption changes, and these two data types have very different spatial sensitivities, causing a poorer sensitivity to deeper regions than that obtained with dual-phase slope data alone.

5. CONCLUSIONS

Our study on the sensitivity of single-distance data types and derived slopes to focal absorption changes has demonstrated the advantages of a dual-slope method. While the spatial resolution in diffuse optics is intrinsically limited by the high ratio (a few hundred) between source-detector separation and scattering mean free path, we have shown a family of source-detector configurations that achieve a deeper and more localized region of sensitivity than with typical source-detector configurations used in diffuse optics. In particular, a 55 mm linear array of two sources and two detectors allows for the determination of dual-slope intensity and phase data with maximal sensitivity at a depth of 5 mm and 11 mm, respectively, under typical conditions of NIRS of blood-perfused tissue. This is a marked improvement over the maximal sensitivity at depths of <2 mm and <5 mm for single-distance intensity and phase data, respectively. This result points to more effective noninvasive measurements of brain and skeletal muscle under superficial layers of skin, skull, adipose tissue, etc.

In addition to a deeper sensitivity, the proposed dual-slope method features significant practical advantages that were previously demonstrated in a self-calibrating approach for absolute measurements of optical properties [15]. These advantages include an insensitivity to instrumental drifts (source emission properties or detector sensitivity response) and variable opto-mechanical coupling between optical probe and tissue (as may result from subject movement or probe adjustment over time) that occurs over a longer time scale than the time resolution of data collection. This is a crucially important feature to enhance the reliability of the data collected on living tissue over relatively long periods of time on moving subjects.

Acknowledgments

REFERENCES

1. Herold F, Wiegel P, Scholkmann F, and Müller NG, "Applications of functional near-infrared spectroscopy (fNIRS) neuroimaging in exercise-cognition science: a systematic, methodology-focused review," J. Clin. Med 7, 466 (2018).

2. Nielsen HB, "Systematic review of near-infrared spectroscopy determined cerebral oxygenation during non-cardiac surgery," Front. Physiol 5, 1–15 (2014). [PubMed: 24478714]

3. la Cour A, Greisen G, and Hyttel-Sorensen S, "In vivo validation of cerebral near infrared spectroscopy: a review," Neurophotonics 5, 040901 (2018). [PubMed: 30525059]

4. Yang M, Yang Z, Yuan T, Feng W, and Wang P, "A systemic review of functional near-infrared spectroscopy for stroke: current application and future directions," Front. Neurol 10, 58 (2019). [PubMed: 30804877]

5. Wolf M, Naulaers G, van Bel F, Kleiser S, and Greisen G, "A review of near infrared spectroscopy for term and preterm newborns," J. Near Infrared Spectrosc 20, 43–55 (2012).

6. Jones S, Chiesa ST, Chaturvedi N, and Hughes AD, "Recent developments in near-infrared spectroscopy (NIRS) for the assessment of local skeletal muscle microvascular function and capacity to utilise oxygen," Artery Res. 16, 25–33 (2016). [PubMed: 27942271]

7. Grosenick D, Rinneberg H, Cubeddu R, and Taroni P, "Review of optical breast imaging and spectroscopy," J. Biomed. Opt 21, 091311 (2016). [PubMed: 27403837]

8. Hoshi Y and Yamada Y, "Overview of diffuse optical tomography and its clinical applications," J. Biomed. Opt 21, 091312 (2016). [PubMed: 27420810]

9. Fantini S, Franceschini MA, Fishkin JB, Barbieri B, and Gratton E, "Quantitative determination of the absorption spectra of chromophores in strongly scattering media: a light-emitting-diode based technique," Appl. Opt 33, 5204–5213 (1994). [PubMed: 20935909]

10. Fantini S, Franceschini-Fantini MA, Maier JS, Walker SA, Barbieri B, and Gratton E, "Frequency-domain multichannel optical detector for non-invasive tissue spectroscopy and oximetry," Opt. Eng 34, 32–42 (1995).

11. Carp SA, Farzam P, Redes N, Hueber DM, and Franceschini MA, "Combined multi-distance frequency domain and diffuse correlation spectroscopy system with simultaneous data acquisition and real time analysis," Biomed. Opt. Express 8, 3993–4006 (2017). [PubMed: 29026684]

12. Suzuki S, Takasaki S, Ozaki T, and Kobayashi Y, "Tissue oxygenation monitor using NIR spatially resolved spectroscopy," Proc. SPIE 3597, 582–592 (1999).

13. Phan P, Highton D, Lai J, Smith M, Elwell C, and Tachtsidis I, "Multi-channel multi-distance broadband near infrared spectroscopy system to measure the spatial response of cellular oxygen metabolism and tissue oxygenation," Biomed. Opt. Express 7, 4424–4440 (2016). [PubMed: 27895985]

14. Franceschini MA, Fantini S, Paunescu LA, Maier JS, and Gratton E, "Influence of a superficial layer in the quantitative spectroscopic study of strongly scattering media," Appl. Opt 37, 7447–7458 (1998). [PubMed: 18301579]

15. Hueber DM, Fantini S, Cerussi AE, and Barbieri BB, "New optical probe designs for absolute (self-calibrating) NIR tissue hemoglobin measurements," Proc. SPIE 3597, 618–631 (1999).

16. Kleiser S, Ostojic D, and Nasseri N, "In vivo precision assessment of a near-infrared spectroscopy-based tissue oximeter (OxyPrem v1.3) in neonates considering systemic hemodynamic fluctuations," J. Biomed. Opt 23, 067003 (2018).

17. Kleiser S, Nasseri N, Andresen B, Greisen G, and Wolf M, "Comparison of tissue oximeters on a liquid phantom with adjustable optical properties," Biomed. Opt. Express 7, 2973–2992 (2016). [PubMed: 27570691]

18. Metz AJ, Pugin F, Huber R, Acherman P, and Wolf M, "Changes of cerebral tissue oxygen saturation at sleep transitions in adolescents," in Oxygen Transport to Tissue XXXVI, Swartz HM, Harrison DK, and Bruley DF, eds., Advances in Experimental Medicine and Biology (Springer, 2014), Vol. 812, pp. 279–285.

19. Jenny C, Biallas M, Trajkovic I, Fauchè J-C, Bucher HU, and Wolf M, "Reproducibility of cerebral tissue oxygen saturation measurements by near-infrared spectroscopy in newborn infants," J. Biomed. Opt 16, 097004 (2011). [PubMed: 21950939]

20. Hyttel-Sorensen S, Sorensen LC, Riera J, and Greisen G, "Tissue oximetry: a comparison of mean values of regional tissue saturation, reproducibility and dynamic range of four NIRS-instruments on the human forearm," Biomed. Opt. Express 2, 3047–3057 (2011). [PubMed: 22076266]

21. Chincarini M, Qiu L, Spinelli L, Torricelli A, Minero M, Dalla Costa E, Mariscoli M, Ferri N, Giammarco M, and Vignola G, "Evaluation of sheep anticipatory response to a food reward by means of functional near-infrared spectroscopy," Animals 9, 11 (2019).

22. Raoult C and Gygax L, "Valence and intensity of video stimuli of dogs and conspecifics in sheep: approach-avoidance, operant response, and attention," Animals 8, 121 (2018).

23. Xu RX, Qiang B, Mao JJ, and Povoski SP, "Development of a handheld near-infrared imager for dynamic characterization of in vivo biological tissue systems," Appl. Opt 46, 7442–7451 (2007). [PubMed: 17952180]

24. Scholkmann F, Metz AJ, and Wolf M, "Measuring tissue hemodynamics and oxygenation by continuous-wave functional near-infrared spectroscopy–how robust are the different calculation methods against movement artifacts?" Physiol. Meas 35, 717–734 (2014). [PubMed: 24622337]

25. Metz A, Wolf M, Achermann P, and Scholkmann F, "A new approach for automatic removal of movement artifacts in nearinfrared spectroscopy time series by means of acceleration data," Algorithms 8, 1052–1075 (2015).

26. Fantini S, "Dynamic model for the tissue concentration and oxygen saturation of hemoglobin in relation to blood volume, flow velocity, and oxygen consumption: Implications for functional

neuroimaging and coherent hemodynamics spectroscopy (CHS)," NeuroImage 85, 202–221 (2014). [PubMed: 23583744]

27. Gu H, Lu H, Ye FQ, Stein EA, and Yanga Y, "Noninvasive quantification of cerebral blood volume in humans during functional activation," NeuroImage 30, 377–387 (2006). [PubMed: 16278086]

28. Fantini S, Hueber D, Franceschini MA, Gratton E, Rosenfeld W, Stubblefield PG, Maulik D, and Stankovic MR, "Non-invasive optical monitoring of the newborn piglet brain using continuous-wave and frequency-domain spectroscopy," Phys. Med. Biol 44, 1543–1563 (1999). [PubMed: 10498522]

29. Sassaroli A, Martelli F, and Fantini S, "Perturbation theory for the diffusion equation by use of the moments of the generalized temporal point-spread function. I. Theory," J. Opt. Soc. Am. A 23, 2105–2118 (2006).

30. Sassaroli A, Martelli F, and Fantini S, "Perturbation theory for the diffusion equation by use of the moments of the generalized temporal point-spread function. III. Frequency-domain and time-domain results," J. Opt. Soc. Am. A 27, 1723–1742 (2010).

31. Delpy DT, Cope M, van der Zee P, Arridge S, Wray S, and Wyatt J, "Estimation of optical path length through tissue from direct time of flight measurements," Phys. Med. Biol 33, 1433–1442 (1988). [PubMed: 3237772]

32. Sassaroli A and Fantini S, "Comment on the modified Beer-Lambert law for scattering media," Phys. Med. Biol 49, N255–N257 (2004). [PubMed: 15357206]

33. Hiraoka M, Firbank M, Essenpreis M, Cope M, Arridge SR, van der Zee P, and Delpy DT, "A Monte Carlo investigation of optical pathlength in inhomogeneous tissue and its application to near-infrared spectroscopy," Phys. Med. Biol 38, 1859–1876 (1993). [PubMed: 8108489]

34. Strangman G, Franceschini MA, and Boas DA, "Factors affecting the accuracy of near-infrared spectroscopy concentration calculations for focal changes in oxygenation parameters," NeuroImage 18, 865–879 (2003). [PubMed: 12725763]

35. Zheng F, Sassaroli A, and Fantini S, "Phasor representation of oxyand deoxyhemoglobin concentrations: what is the meaning of out-of-phase oscillations as measured by near-infrared spectroscopy?" J. Biomed. Opt 15, 040512 (2010). [PubMed: 20799778]

36. Contini D, Martelli F, and Zaccanti G, "Photon migration through a turbid slab described by a model based on diffusion approximation. I. Theory," Appl. Opt 36, 4587–4599 (1997). [PubMed: 18259254]

37. Bigio IJ and Fantini S, Quantitative Biomedical Optics: Theory, Methods, and Applications (Cambridge University, 2016).

38. Martelli F, Del Bianco S, Ismaelli A, and Zaccanti G, Light Propagation in Biological Tissues and Other Diffusive Media (SPIE Press, 2010)

39. Feng S, Zeng F, and Chance B, "Photon migration in the presence of a single defect–a perturbation analysis," Appl. Opt 34, 3826–3837 (1995). [PubMed: 21052207]

40. Fantini S, Franceschini MA, Walker SA, Maier JS, and Gratton E, "Photon path distributions in turbid media: applications for imaging," Proc. SPIE 2389, 340–349 (1995).

41. Hallacoglu B, Trobaugh JW, Bechtel KL, and Seshagiri CV, "Blood phantom verification for a new compact DOT system," in Biomedical Optics 2016 (Optical Society of America, 2016), paper JM3A.3.

42. Tgavalekos K, Pham T, Krishnamurthy N, Sassaroli A, and Fantini S, "Frequency-resolved analysis of coherent oscillations of local cerebral blood volume, measured with near-infrared spectroscopy, and systemic arterial pressure in healthy human subjects," PLOS One 14, e0211710 (2019). [PubMed: 30753203]

43. Blaney G, Sassaroli A, Pham T, Fernandez C, and Fantini S, "Phase dual-slopes in frequency-domain near-infrared spectroscopy for enhanced sensitivity to brain tissue: first applications to human subjects," J. Biophotonics (to be published).
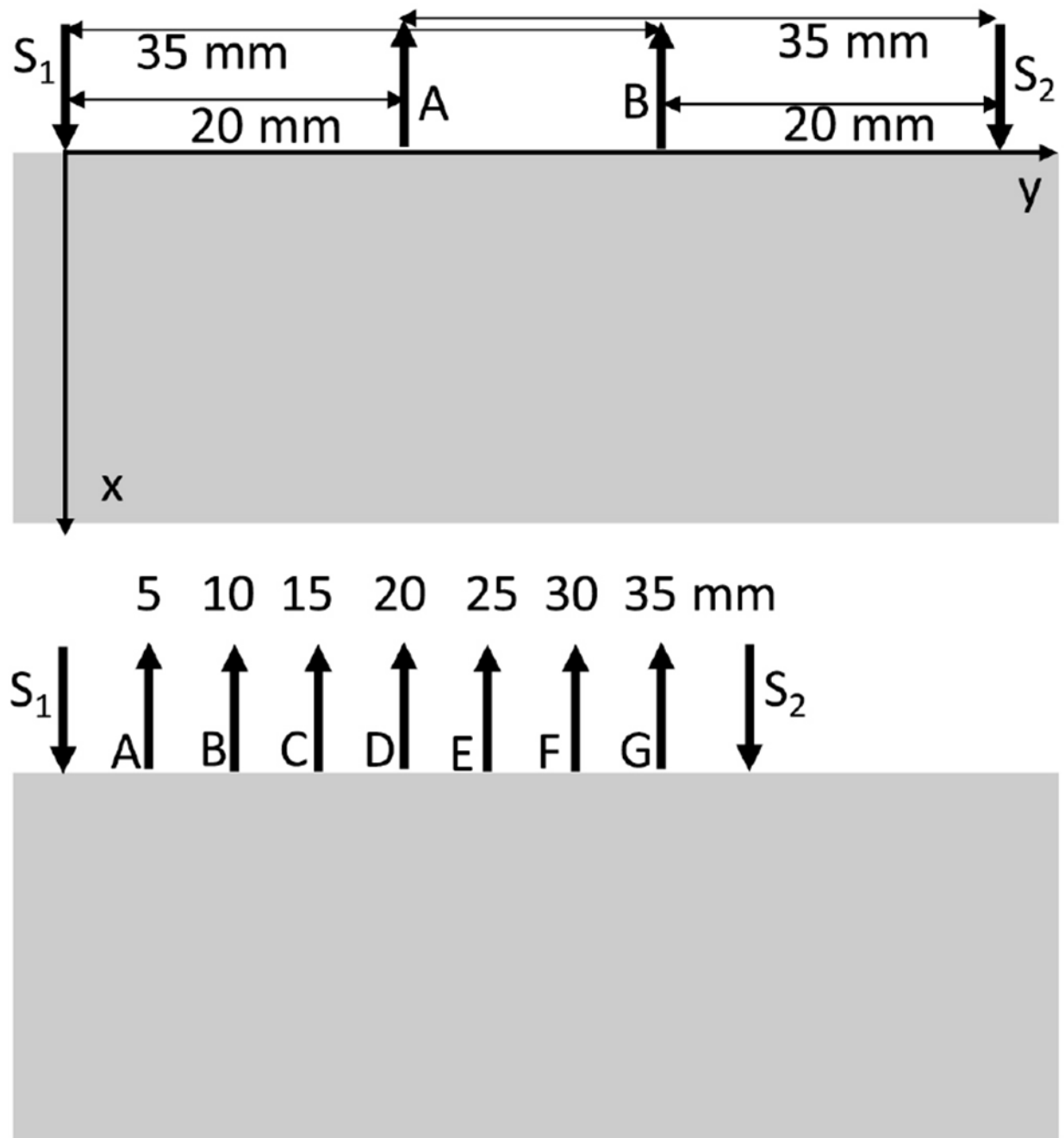
Fig. 1.
Top panel: linear source-detector arrangement for the dual-slope method with two sources (S$_1$ and S$_2$) and two detectors (A and B). Bottom panel: extended dual-slope method using two sources and seven detectors (A–G). In the bottom panel the distances are calculated with respect to the source S$_1$. Given the symmetric arrangement, these are also the distances between the detectors and S$_2$ but in the reverse order. Note that the x axis is the depth coordinate, while the y axis is along the line that contains all sources and detectors.
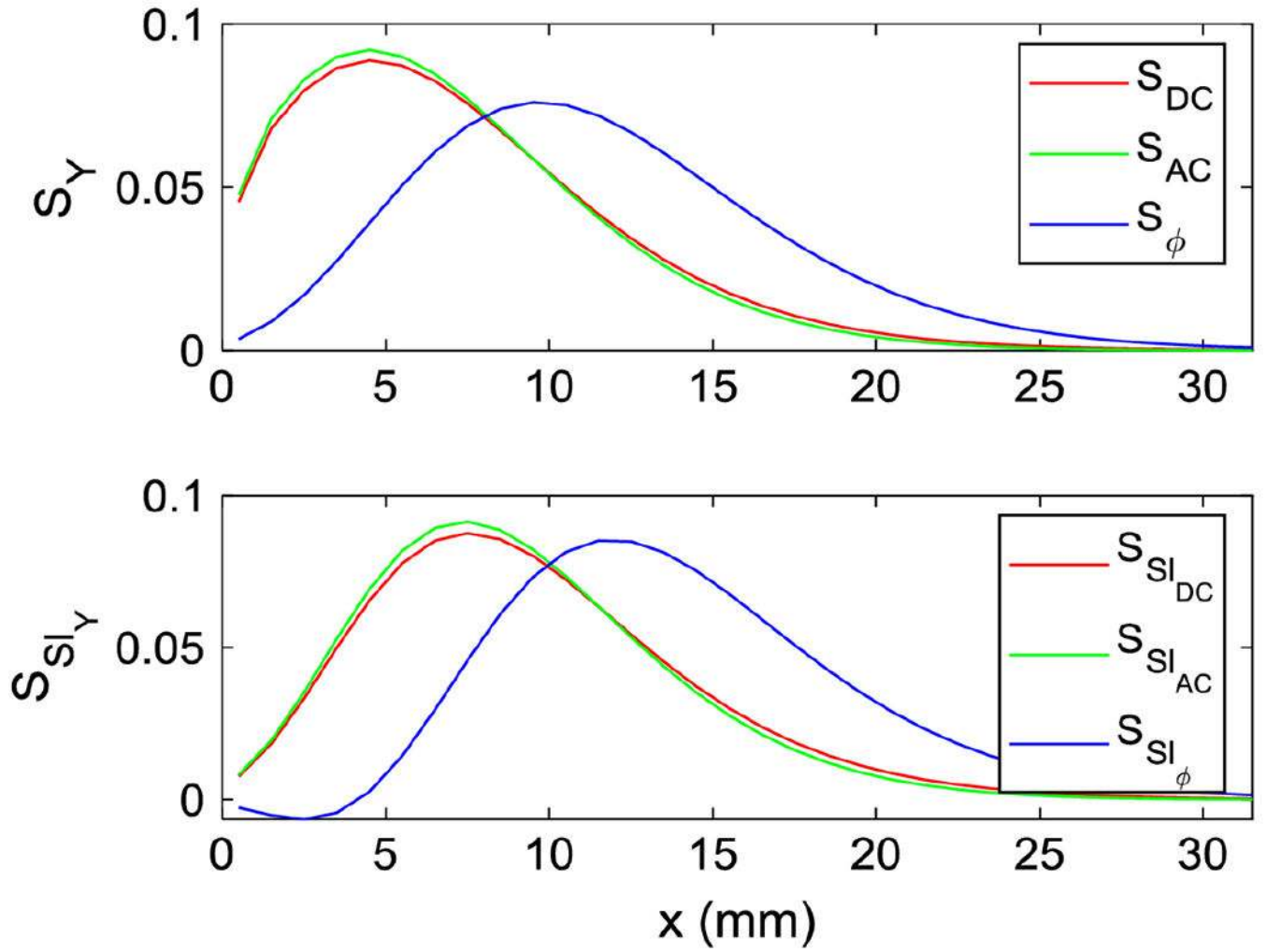
Fig. 2.

Sensitivity of raw data at a single-distance S_Y (top panel) and their slopes S_{SlY} (bottom panel) according to Eqs. (10) and (16), respectively, are obtained for the three data types ("Y": DC intensity, AC amplitude, and φ phase; labeled as "DC", "AC", and "ϕ", respectively) by scanning a layer of size $1 \times 80 \times 80$ mm along the x axis (depth) at 1 mm steps. For layered changes in the absorption coefficient we remind that $S_{SSlY} = S_{DSlY}$. The optical properties of the medium are $\mu_a = 0.01$ mm^{-1}, $\mu'_s = 1$ mm^{-1}. The refractive index of the diffusive medium and the outer medium are $n_i = 1.4$, $n_o = 1$. The modulation frequency is 140 MHz. S_{SlY} were calculated by using the source-detector arrangement of Fig. 1 (top panel), while S_Y refer to the farthest distance (35 mm).
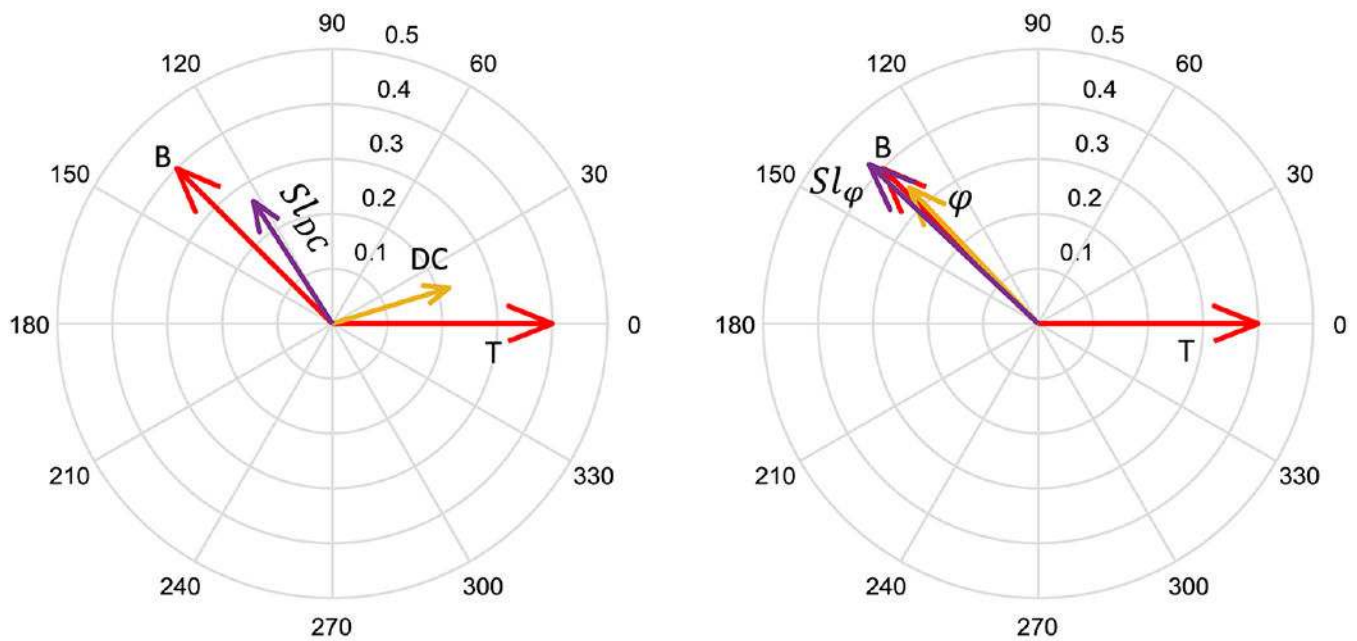
Fig. 3.
Ratio of estimated phasor $\mathbf{D}_E/\mathbf{O}_E$ with DC intensity data and DC intensity slope labeled as "DC" (orange arrow, left panel) and "Sl_{DC}" (purple arrow, left panel), respectively. Phase data and phase slope data are labeled as "φ" (orange arrow, right panel) and "Sl_φ" (purple arrow, right panel), respectively. The true phasors ratio $\mathbf{D}_T/\mathbf{O}_T$ for the top and bottom layers (red arrows) are indicated by the labels "T" and "B", respectively. The layers are 1 mm thick and occupy the regions [0, 1] mm and [15, 16] mm, for "T" and "B", respectively. We remind that for layered changes in absorption $S_{SSlY} = S_{DSlY}$; therefore, it is unnecessary to specify if we are considering single or dual slopes.
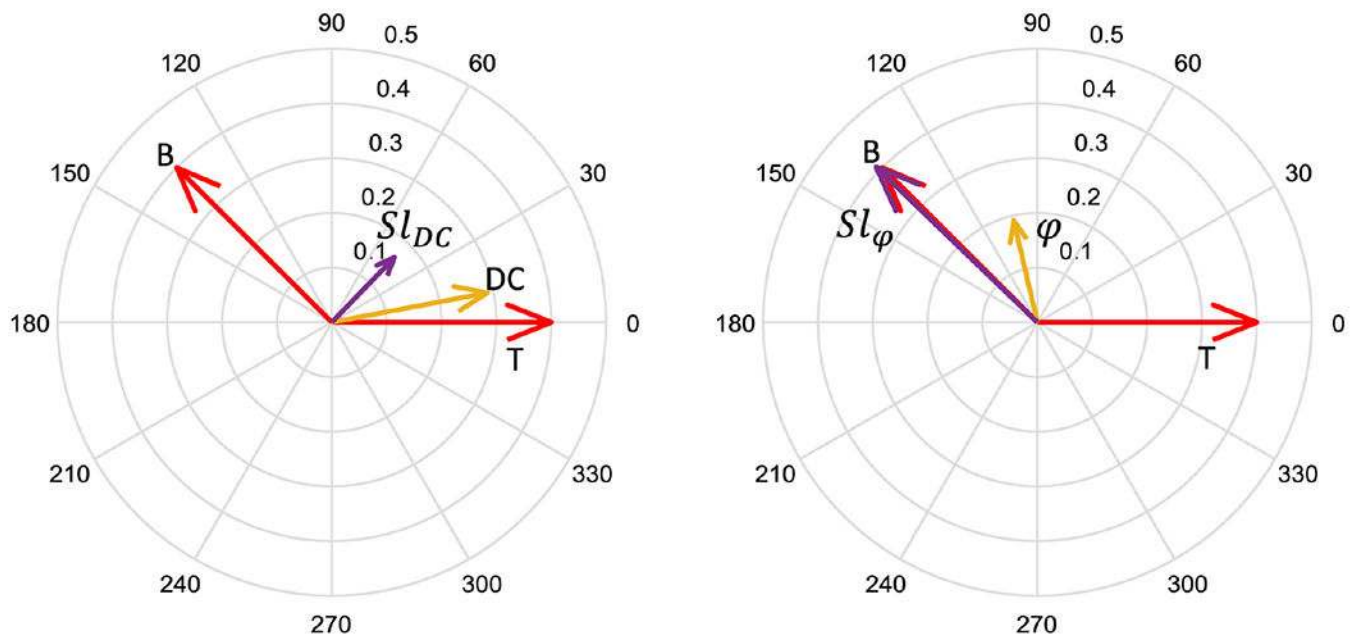
Fig. 4.
Ratio of estimated phasor $\mathbf{D}_E/\mathbf{O}_E$ with DC intensity data and DC intensity slope indicated as "DC" (orange arrow, left panel) and "Sl_{DC}" (purple arrow, left panel), respectively. Phase data and phase slope data indicated as "φ" (orange arrow, right panel) and "Sl_φ" (purple arrow, right panel), respectively. The true phasors ratio $\mathbf{D}_T/\mathbf{O}_T$ for the top and bottom layers (red arrows) are indicated by the labels "T" and "B," respectively. The layers are 6 mm thick and occupy the regions [0, 6] mm [12, 18] mm for "S" and "B," respectively. We remind that for layered changes in absorption $S_{SSlY} = S_{DSlY}$; therefore, it is unnecessary to specify if we are considering single or dual slopes.
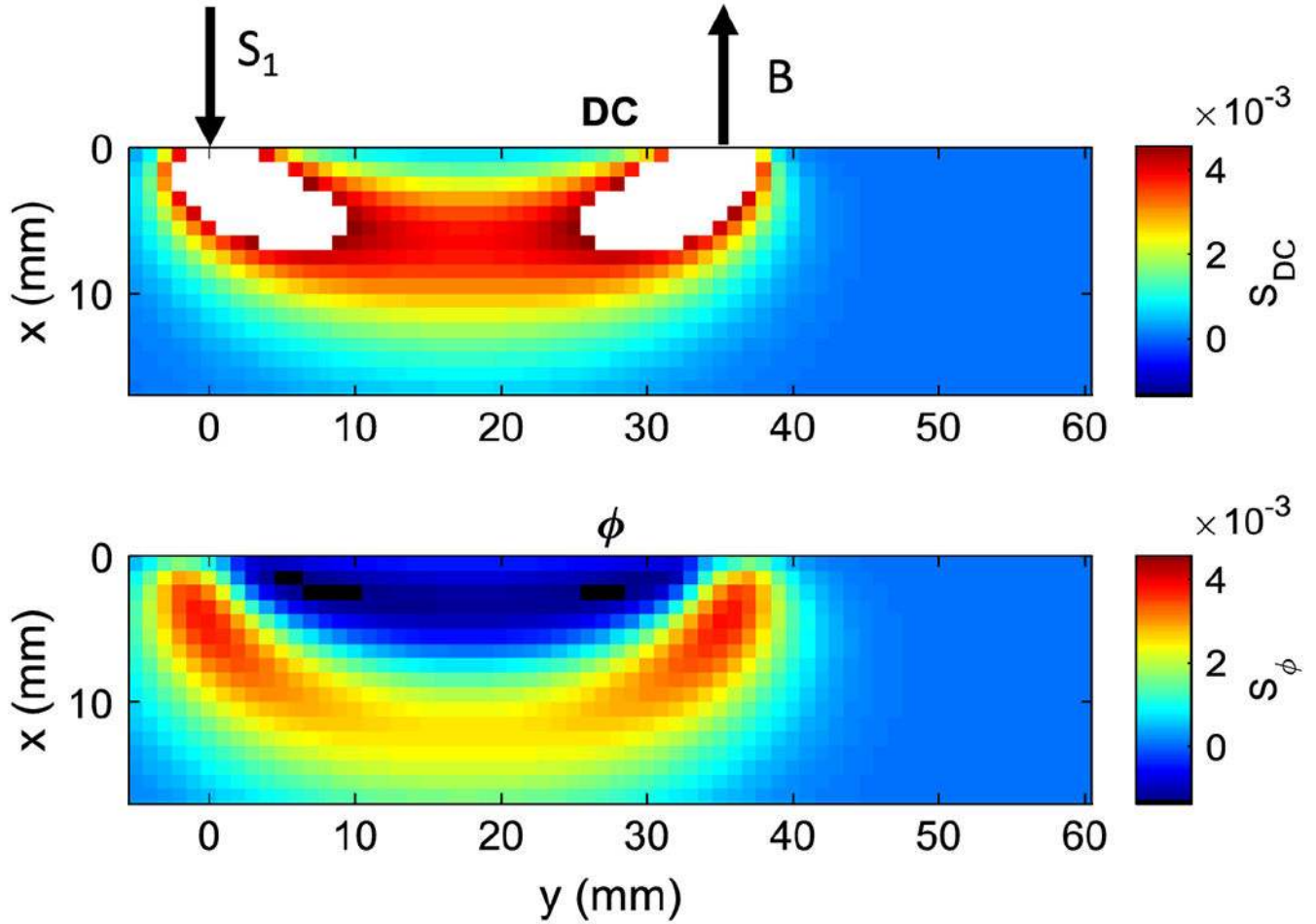
Fig. 5.
Sensitivity maps for single-distance (35 mm) data (S_Y) for two data types ("Y": DC intensity and φ phase) defined in Eq. (10), for DC intensity data (labeled as "DC," top panel), and phase data (labeled as "ϕ," bottom panel). The maps were obtained by scanning a $1 \times 5 \times 5$ mm rectangular cuboid (in the *x, y,* and *z*) direction, along the depth (*x* axis) and horizontal directions (*y* and *z* axis) by steps of 1 mm. The optical properties of the background and modulation frequency were the same as those in Figs. 3 and 4 at 690 nm. The arrows indicate the position of the input source S_1 and detector B (see Fig. 1).
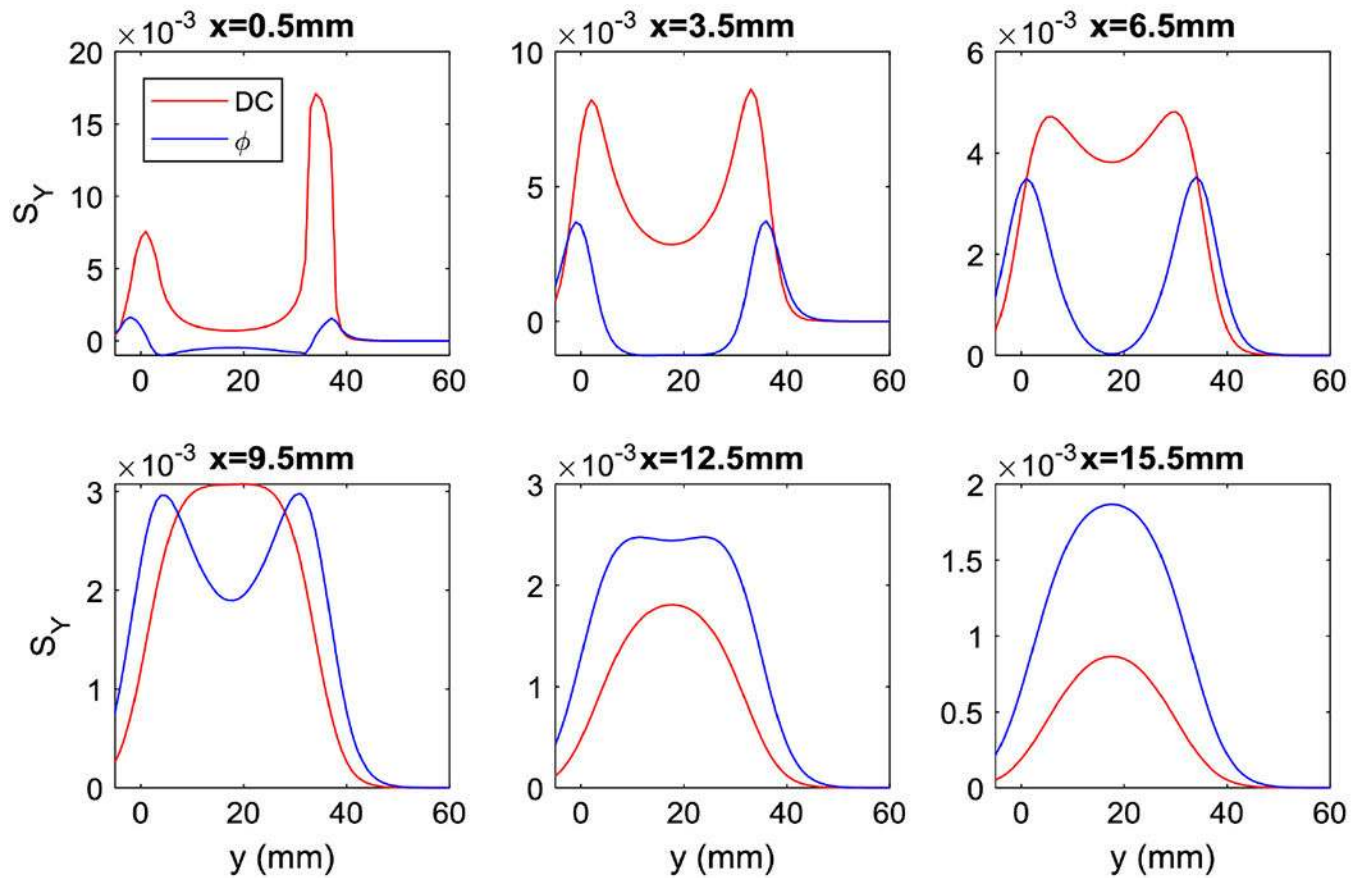
Fig. 6.

Cross-sectional plots along the horizontal direction (y) of the sensitivity (S_Y) maps of Fig. 5 for single-distance data and two data types ("Y": DC intensity and φ phase). Each subplot includes both DC intensity and phase sensitivity (labeled as "DC" and "ϕ," respectively) and it refers to a different depth (x) of the cuboid's center in the medium (indicated on top of each subplot).
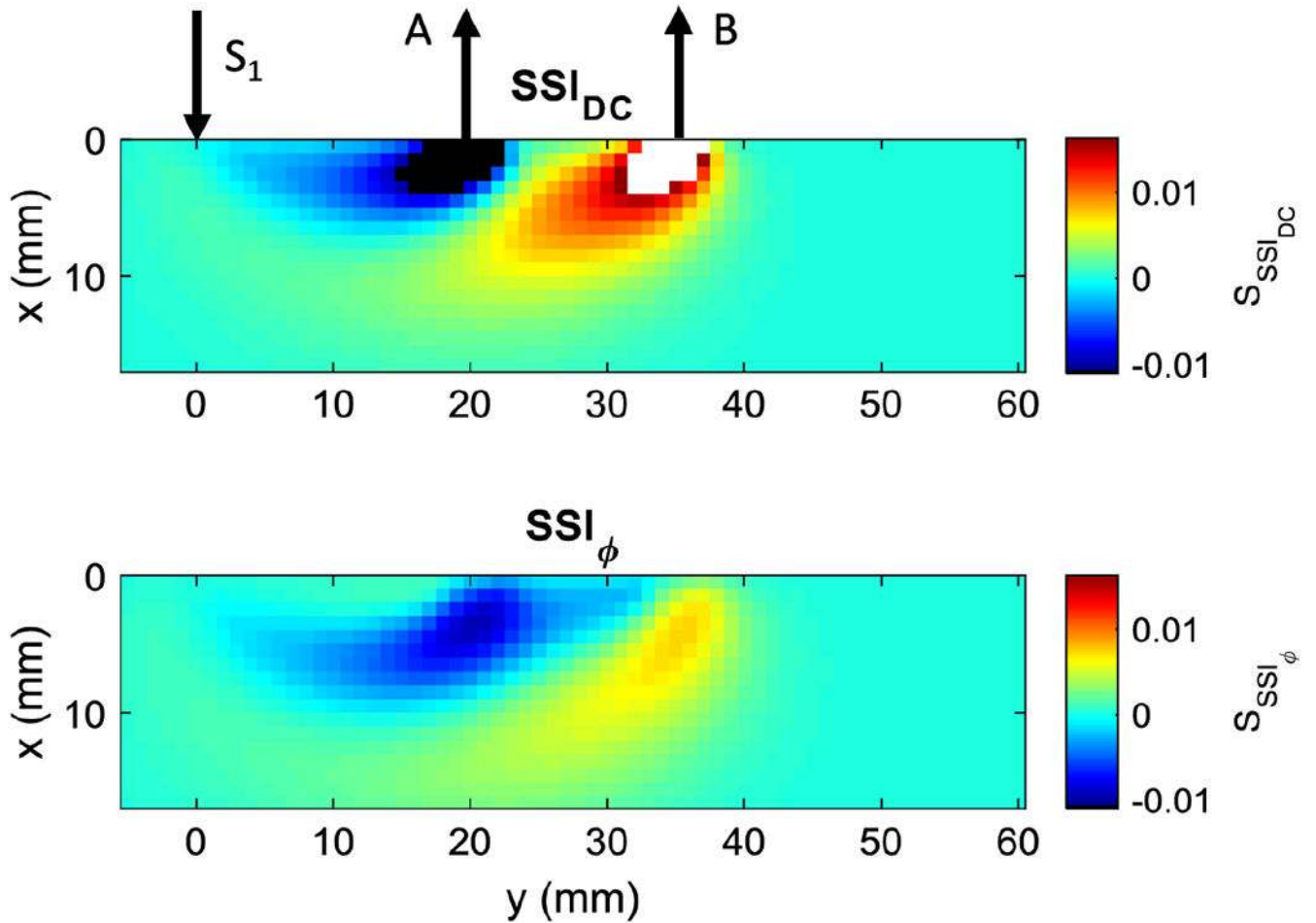
Fig. 7.
Sensitivity maps for single slopes (S_{SSI_Y}) for two data types (" Y ": DC intensity and φ phase) defined in Eq. (16), for DC intensity slope (labeled as "SSI$_{DC}$," top panel) and phase slope (labeled as "SSI$_{\phi}$," bottom panel). They were obtained by scanning a $1 \times 5 \times 5$ mm rectangular cuboid (in the $x, y,$ and z) direction, along the depth (x axis) and horizontal directions (y and z axis) by steps of 1 mm. The optical properties of the background and modulation frequency are the same as those in Figs. 3 and 4 at 690 nm. The slopes were calculated by using the source detectors S_1A and S_1B of Fig. 1 (top panel) (distances: 20 and 35 mm), which are represented by arrows on top of the DC sensitivity map.
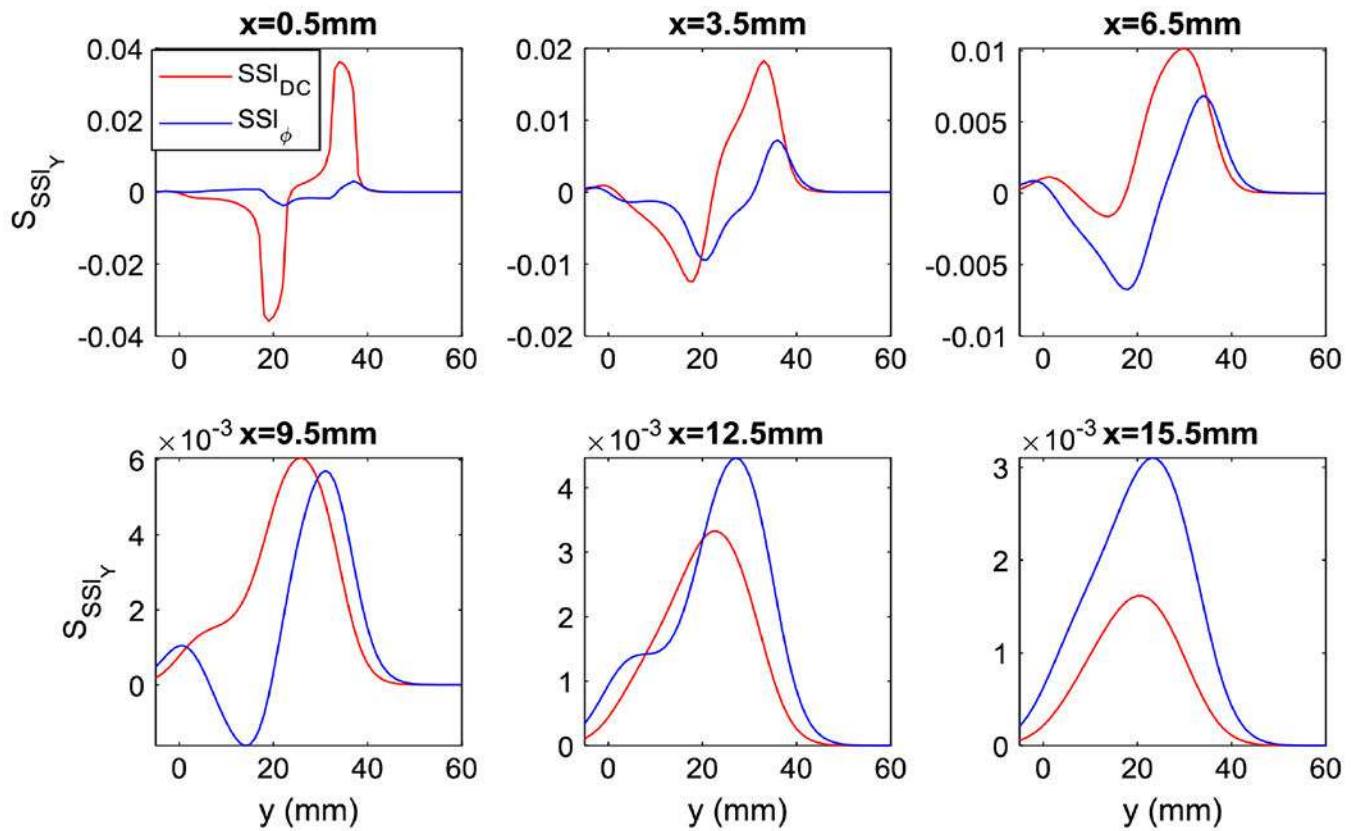
Fig. 8.
Cross-sectional plots along the horizontal direction (y) of the single-slope sensitivity (S_{SSIY}) maps of Fig. 7 for two data types ("Y": DC intensity and φ phase). DC intensity single slope (labeled as "SSl_{DC}") and phase single slopes (labeled as "SSl_ϕ"). Each subplot refers to a different depth (x) of the cuboid's center in the medium (indicated on top of each subplot).
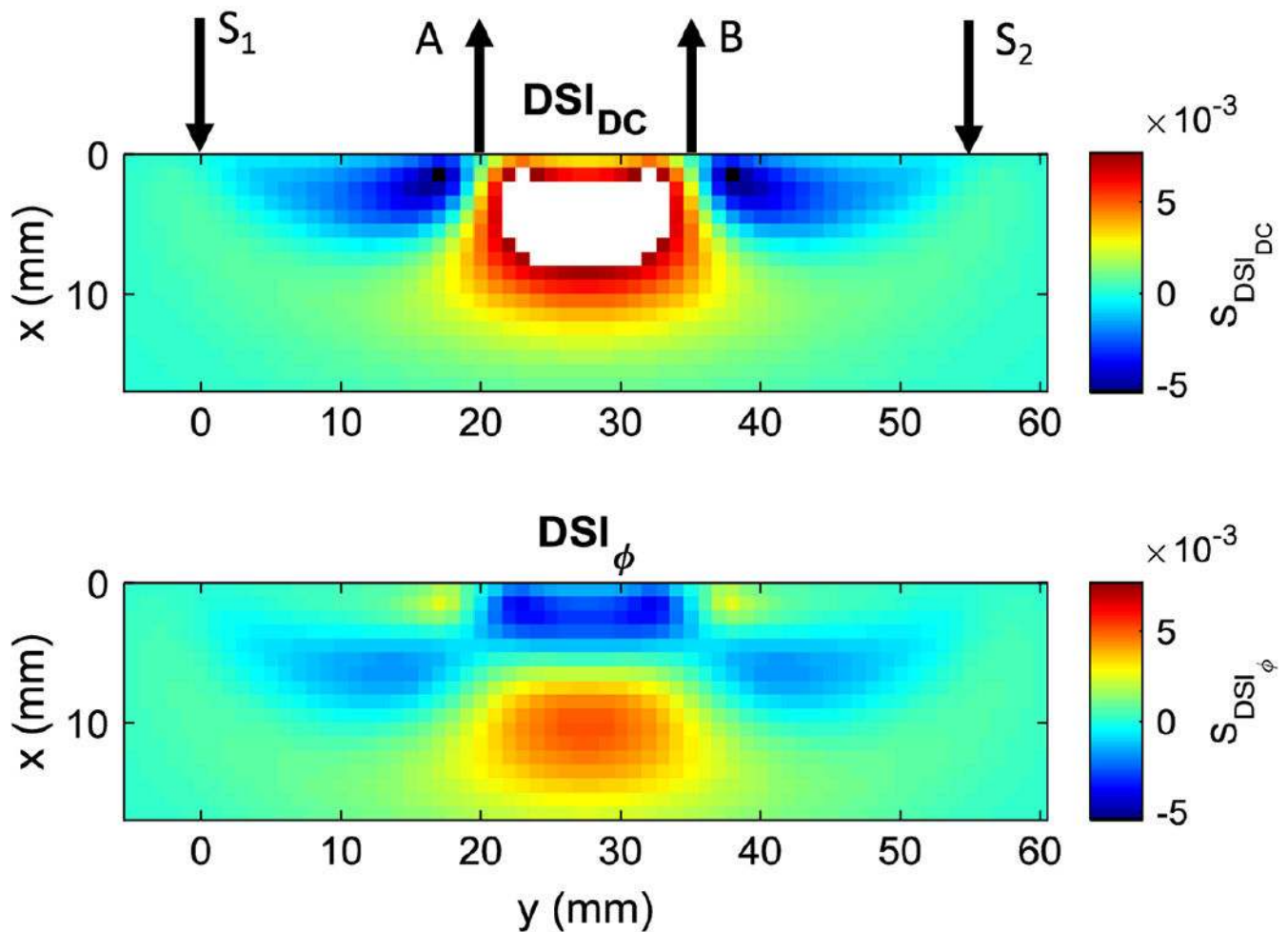
Fig. 9.
Sensitivity maps for dual-slope data (S_{DSl_Y}) for two data types ("Y": DC intensity and φ phase) defined in Eq. (31), for DC intensity dual slope data (labeled as "DSl$_{DC}$," top panel) and phase dual-slope data (labeled as "DSl$_{\phi}$," bottom panel). They were obtained by scanning a $1 \times 5 \times 5$ mm rectangular cuboid (in the x, y, and z) direction, along the depth (x axis) and horizontal directions (y and z axis) by steps of 1 mm. The optical properties of the background were the same as those in Figs. 3 and 4 at 690 nm. The dual slopes were calculated by using the source detectors S_1A and S_1B for one slope and S_2BS_2A for the matched slope [Fig. 1 (top panel)], which are represented by arrows on top of the DC dual-slope sensitivity map.
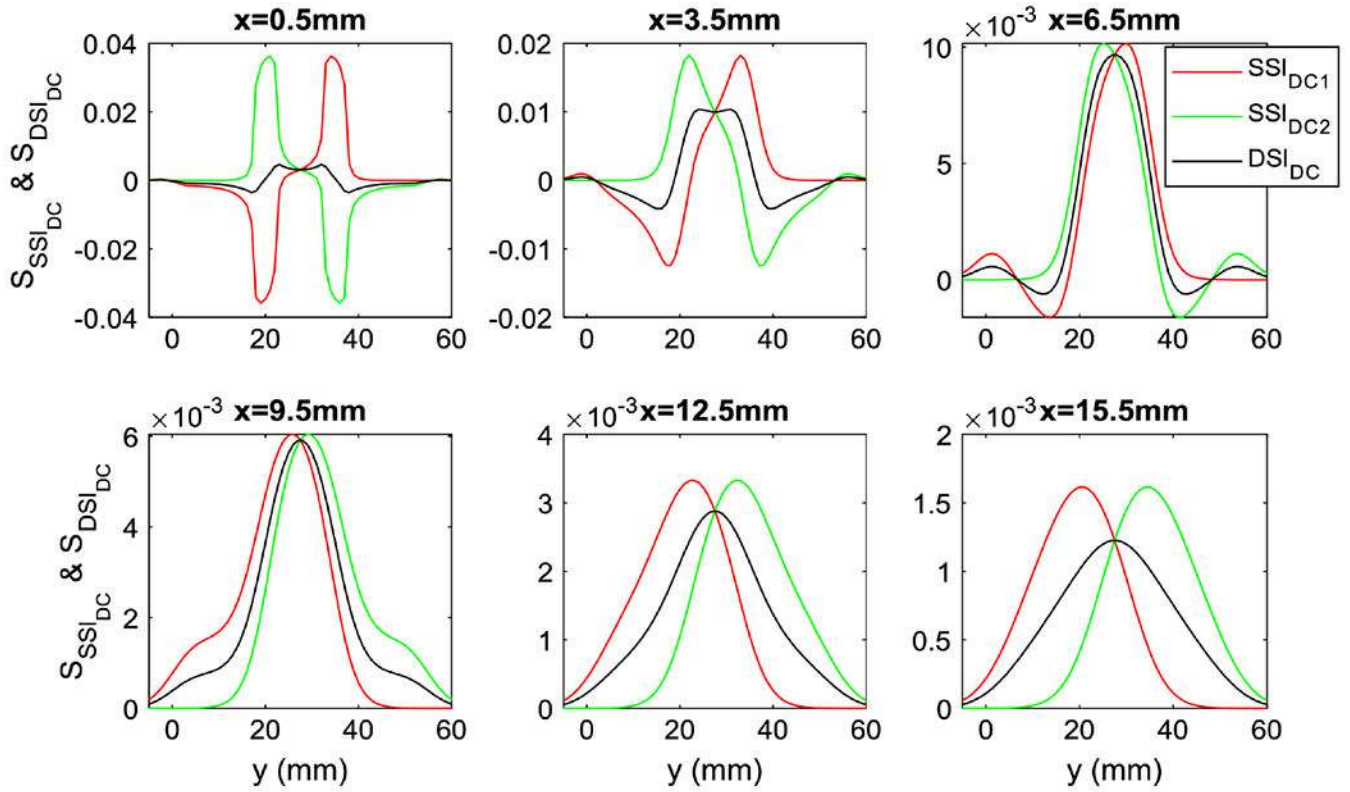
Fig. 10.

Comparison of cross-sectional plots along the horizontal direction (y) of (1) the DC intensity dual-slope sensitivity map of Fig. 9 (black lines labeled as "DSI_{DC}"); (2) the DC intensity single-slope sensitivity map of Fig. 7 calculated with S_1A and S_1B (red lines labeled as "SSI_{DC1}"); (3) the sensitivity maps of the matched DC intensity single slope calculated with S_2B and S_2A (see Fig. 1 top panel) (green lines labeled as "SSI_{DC2}").
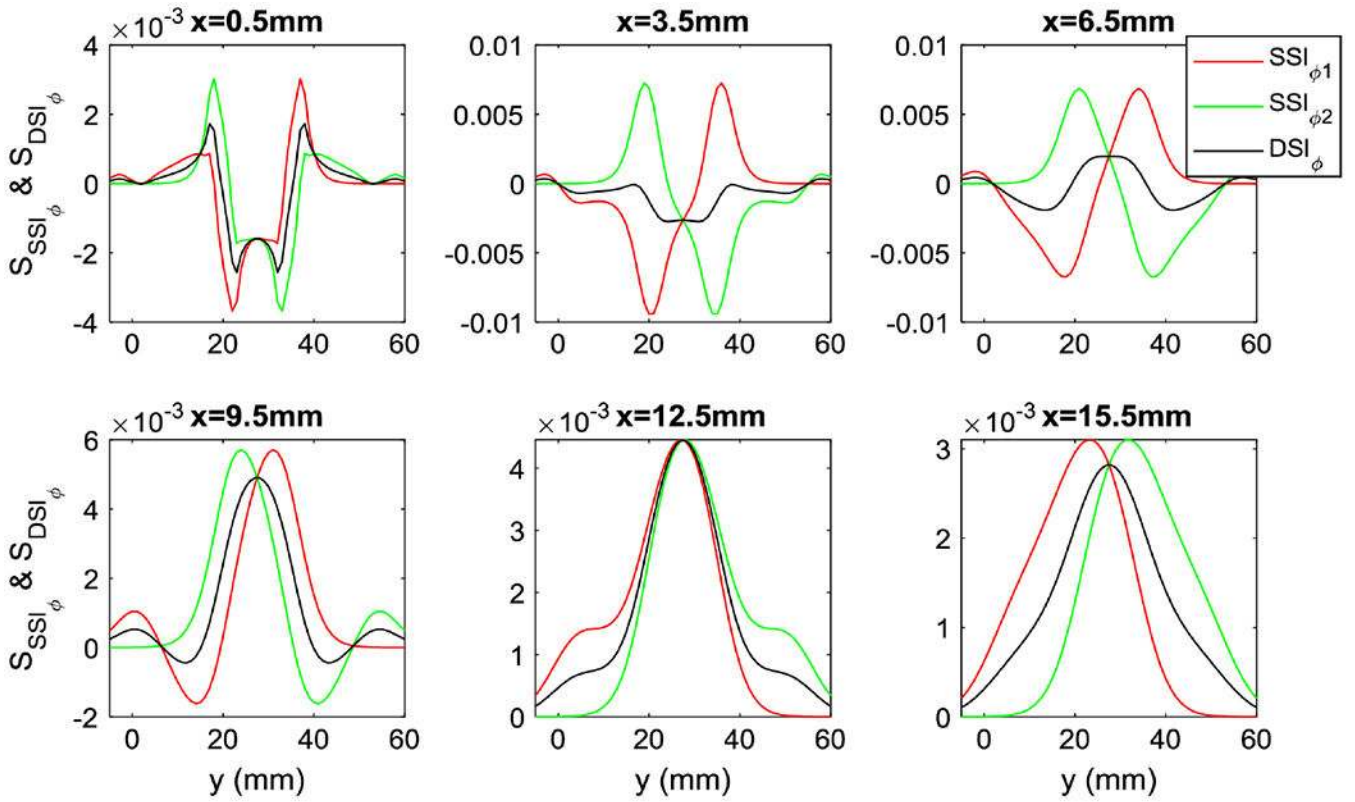
Fig. 11.

Comparison of cross-sectional plots along the horizontal direction (y) of (1) the phase dual-slope sensitivity map of Fig. 9 (black lines labeled as "DSI_ϕ"); (2) the phase single-slope sensitivity map pf Fig. 7 calculated with S_1A and S_1B (red lines labeled as $SSI_{\phi 1}$); (3) the sensitivity maps of the matched phase intensity single slope calculated with S_2B and S_2A (see Fig. 1 top panel) (green lines labeled as "$SSI_{\phi 2}$").
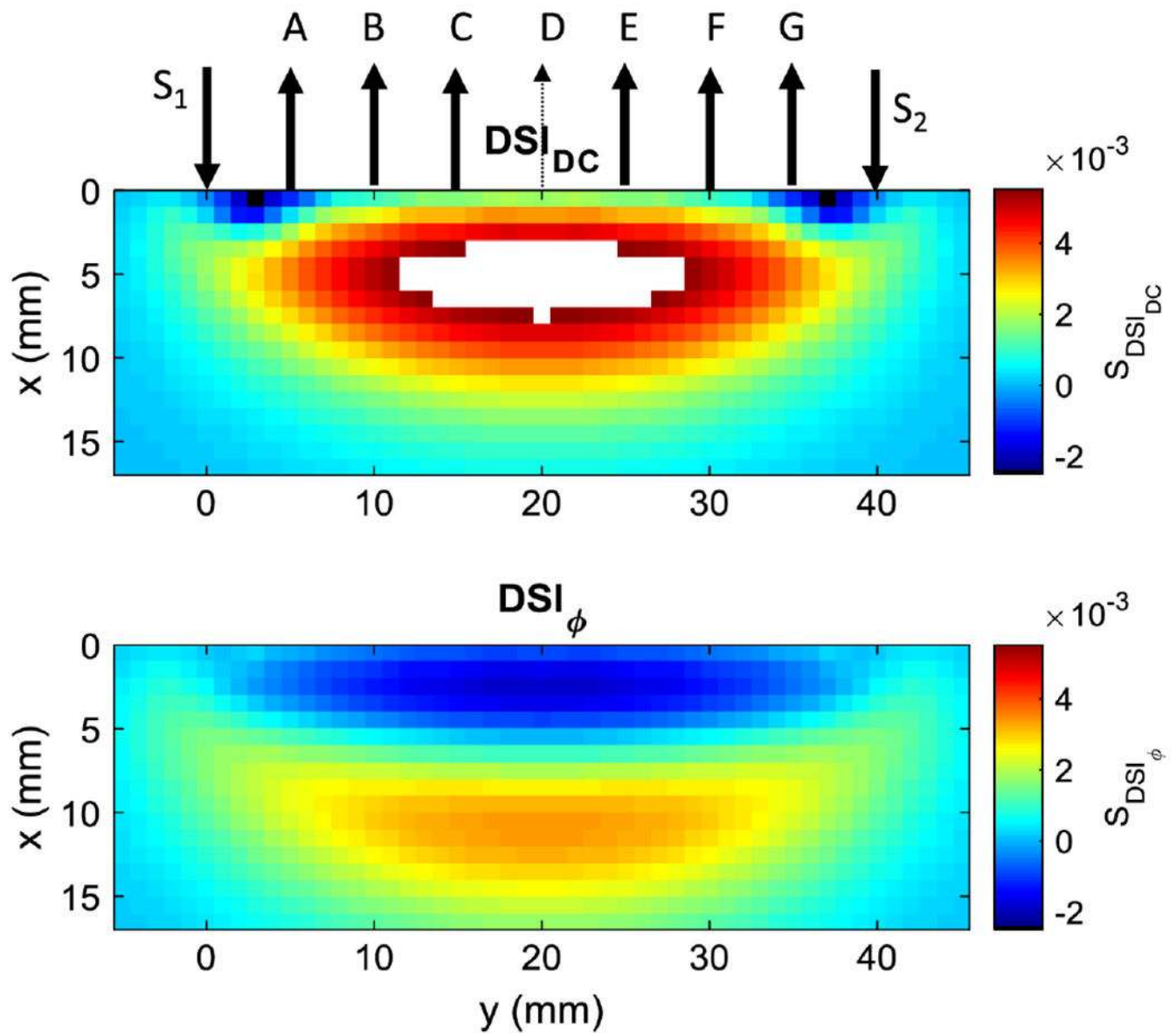
Fig. 12.
Sensitivity maps for dual-slope data ($S_{DSI\,Y}$) for two data types ("Y: DC intensity and φ phase) defined in Eq. (31) for DC intensity dual-slope data (labeled as "DSI_{DC}," top panel) and phase dual-slope data (labeled as "DSI_{ϕ}," bottom panel). Obtained with two sources and seven detectors [Fig. 1 (bottom panel)]. The maps were obtained in the same situation of Fig. 9.
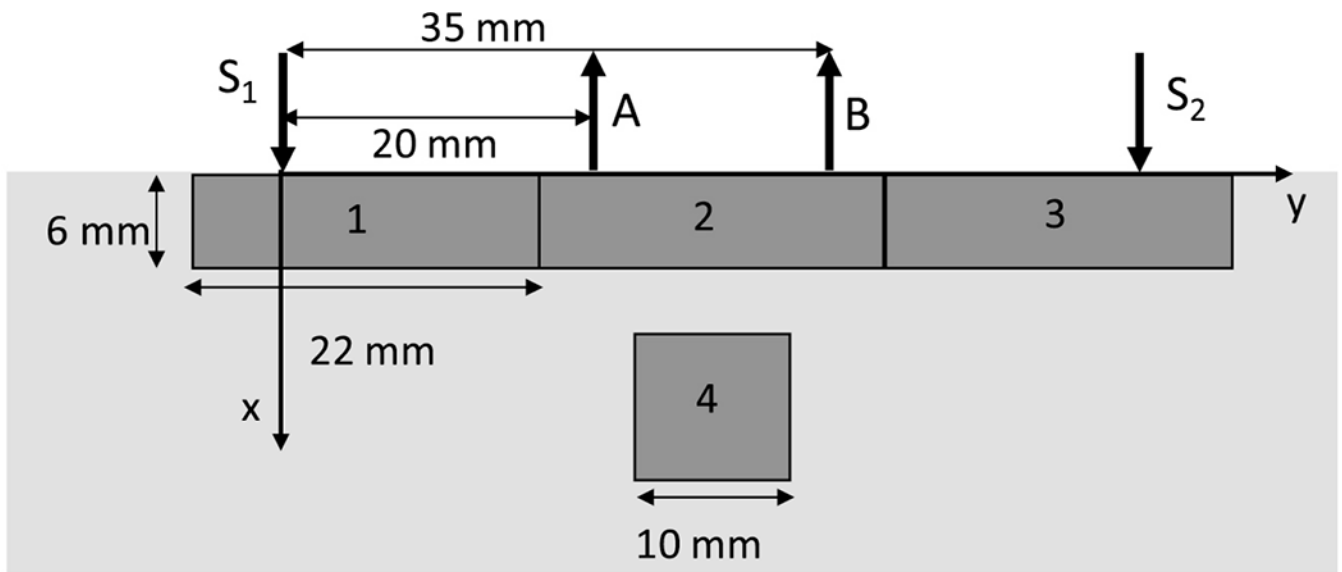
Fig. 13.
Schematic representation of a diffusive medium comprising three equal top regions with size (6,22,40) mm along (x, y, z) and one cubic deeper region of side 10 mm. The centers of the three top regions are (x, y, z) = (3, 5.5, 0) mm (region 1), (x, y, z) = (3, 27.5, 0) mm (region 2), (x, y, z) = (3, 49.5, 0) mm (region 3). The cubic region 4 (10 mm side) is centered at (x, y, z) = (15, 27.5, 0) mm. The source-detector arrangement is the same as in Fig. 1. The background optical properties are the same as those of Fig. 3.
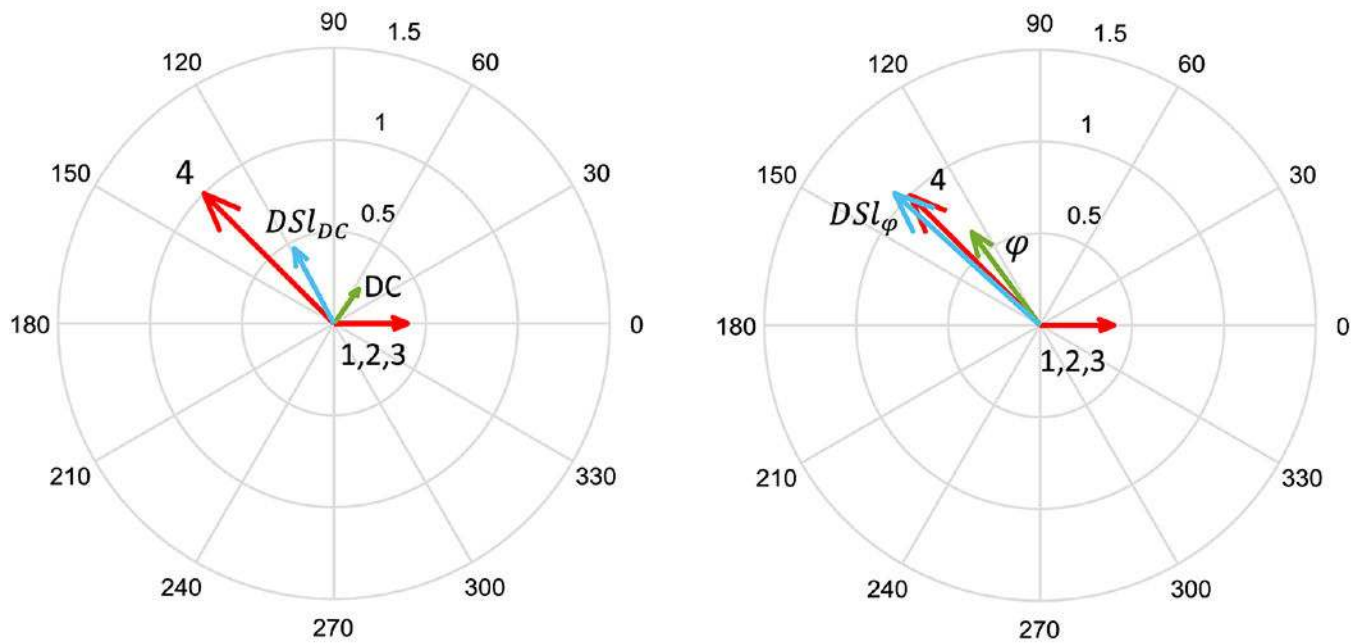
Fig. 14.

First case of the ratio of estimated phasor $\mathbf{D}_E/\mathbf{O}_E$ with single-distance DC intensity data and DC intensity dual slope, labeled "DC" (green arrow, left panel) and "DSl_{DC}" (blue arrow, left panel), respectively. Single-distance phase data and dual-slope phase, labeled "φ" (green arrow, right panel) and "DSl_φ" (blue arrow right panel), respectively (right panel). The true phasor ratio $\mathbf{D}_T/\mathbf{O}_T$ for the three top layers and one deeper region (red arrows) are indicated by the numbers 1, 2, 3, and 4 (see Fig. 13 for the labeling of the four regions). The ratio of phasors obtained with the single slopes (not shown) are almost coincident with those obtained with the dual slopes.
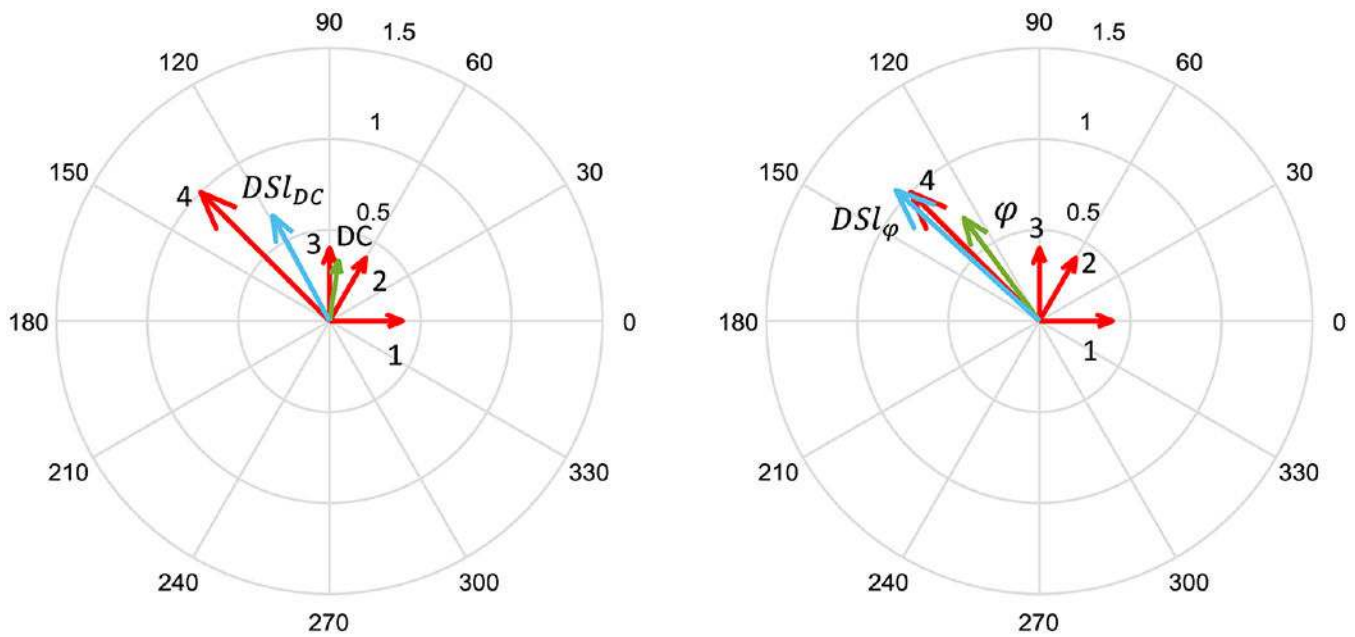
Fig. 15.
Second case of the ratio of estimated phasor $\mathbf{D}_E/\mathbf{O}_E$ with single-distance DC intensity data and DC intensity dual slope, labeled "DC" (green arrow, left panel) and "DSl$_{DC}$" (blue arrow, left panel), respectively. Single-distance phase data and dual-slope phase, labeled "φ" (green arrow, right panel) and "DSl_φ" (blue arrow right panel), respectively (right panel). The true phasor ratio $\mathbf{D}_T/\mathbf{O}_T$ for the three top layers and one deeper region (red arrows) are indicated by the numbers 1, 2, 3, and 4 (see Fig. 13 for the labeling of the four regions). The ratio of phasors obtained with the single slopes (not shown) are almost coincident with those obtained with the dual slopes.
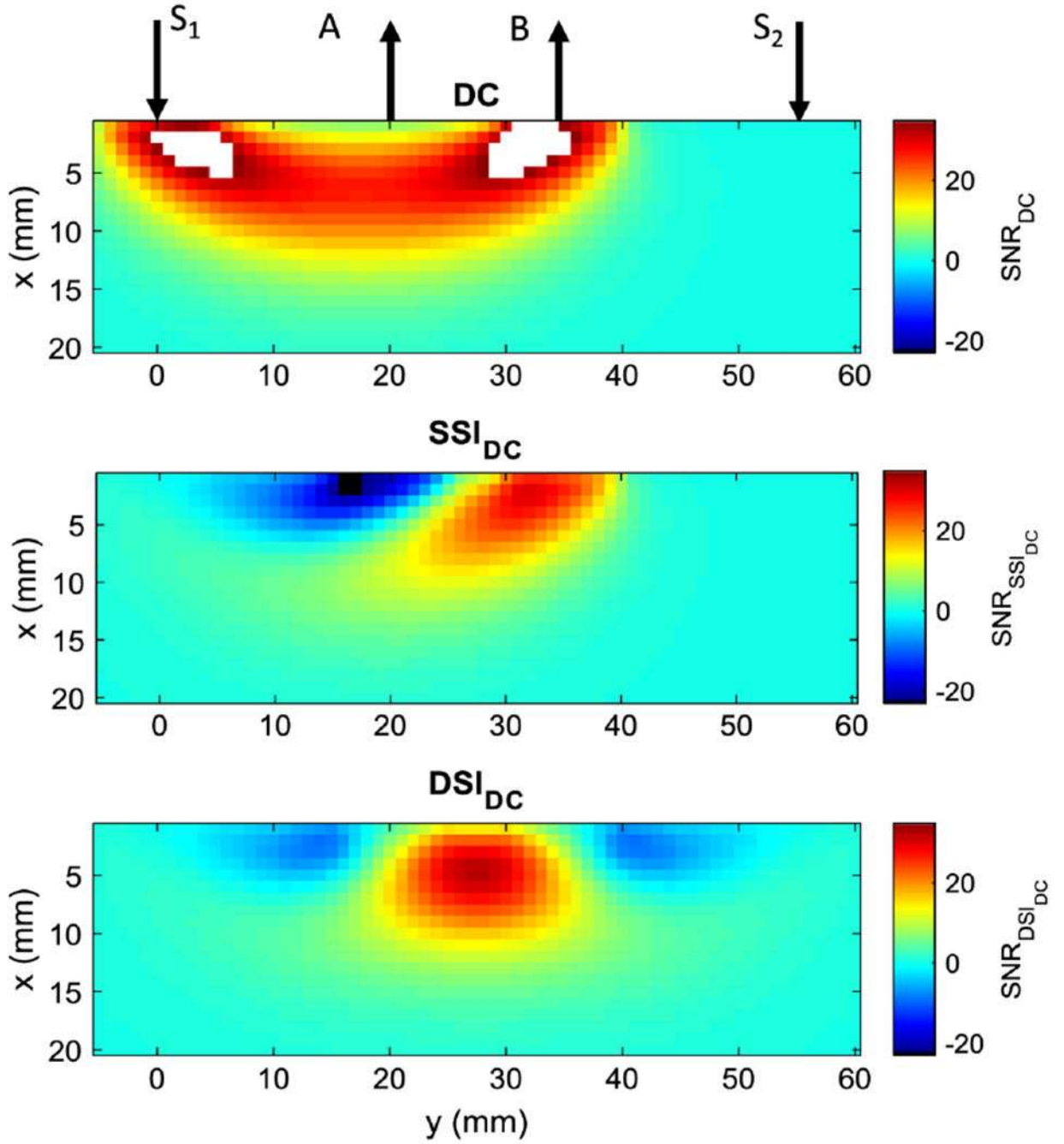
Fig. 16.
Maps of signal-to-noise ratio (SNR) for DC intensity data labeled "DC" (top panel), DC intensity single-slope data labeled "SSI_{DC}" (middle panel), and DC intensity dual-slope data labeled "DSI_{DC}" (bottom panel). Same source detector arrangement shown in Fig. 1 (top panel) with S_1 and S_2 as sources and A and B as detectors (top panel).

Fig. 17.
Maps of signal-to-noise ratio (SNR) for phase (φ) data labeled "ϕ" (top panel), phase single-slope data labeled "SSl$_\phi$" (middle panel), and phase dual-slope data labeled "DSl$_\phi$" (bottom panel). Same source detector arrangement shown in Fig. 1 (top panel) with S_1 and S_2 as sources and A and B as detectors (top panel).
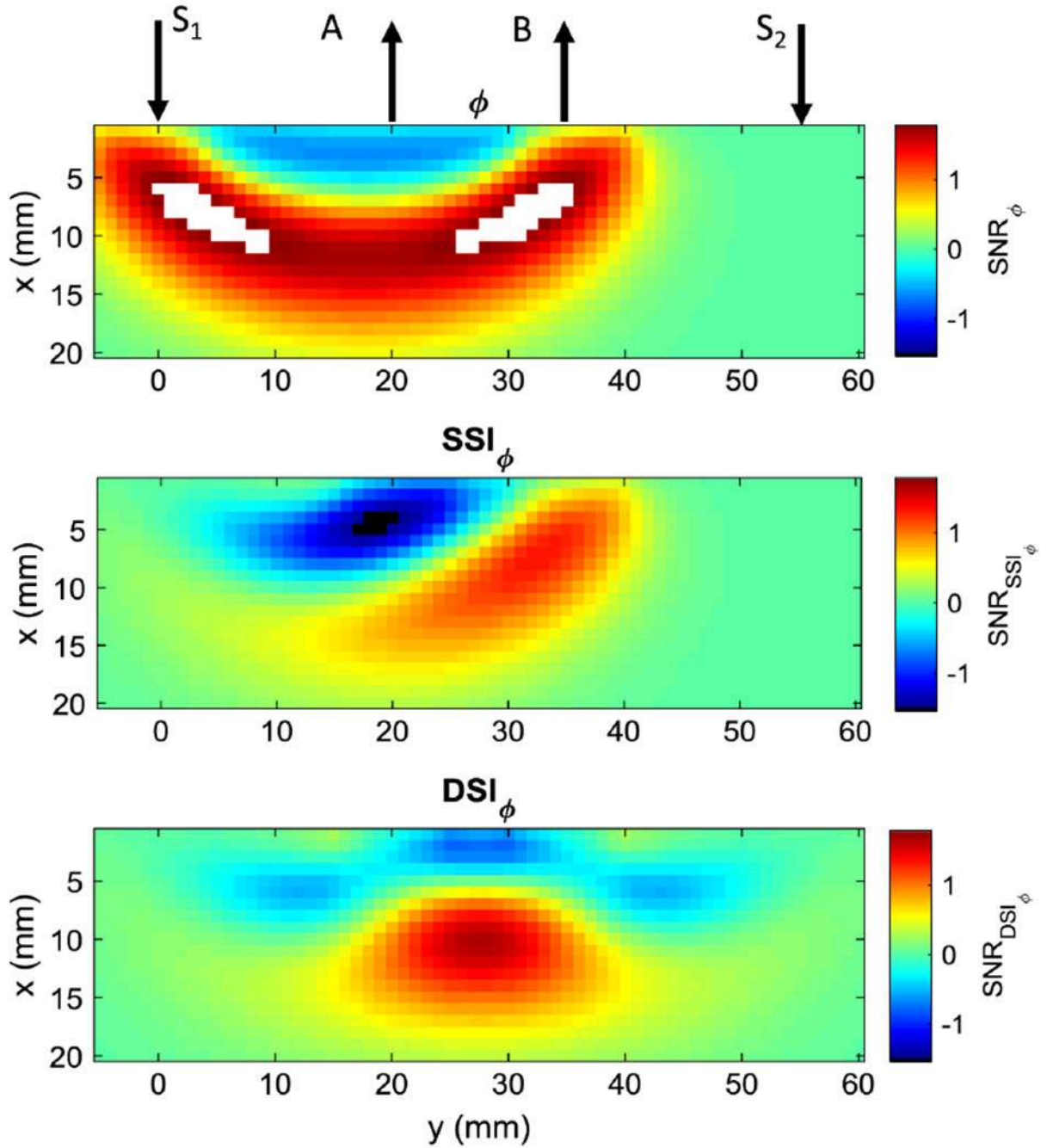
Table 1.

SNR Calculated for the Example of Fig. 15 by Using DC Single-Distance (SNR_{DC}), DC Dual-Slope ($SNR_{DSI_{DC}}$), Phase Single-Distance (SNR_φ), and Phase Dual-Slope (SNR_{DSI_φ})[a]

Region		1	2	3	4
SNR_{DC}	λ_1	18.5 (33%)	17.7 (32%)	<1	19.5 (35%)
	λ_2	17.3 (41%)	17.1 (40%)	<1	7.5 (18%)
$SNR_{DSI_{DC}}$	λ_1	1.15 (4%)	11 (34%)	<1	19 (59%)
	λ_2	<1	10.4 (54%)	<1	7.2 (37%)
SNR_φ	λ_1	<1	<1	<1	3.5 (77%)
	λ_2	<1	<1	<1	1.3 (56%)
SNR_{DSI_φ}	λ_1	<1	<1	<1	3.3 (95%)
	λ_2	<1	<1	<1	1.2 (91%)

[a]The SNR is given for each region and each wavelength (λ_1 = 690 nm and λ_2 = 830 nm) whenever it is larger than 1 (limit of detectability). At the side of each SNR, its percentage with respect to the total SNR is also reported.